Sensors and Actuators B: Chemical, Volume 430, May 2025, Article number 137378
DOI:10.1016/j.snb.2025.137378

Light/Ultrasound Enhance Peroxidase Activity of $BaTiO_3$/graphdiyne/Au Nanozyme for Colorimetric Detection of *E. coli* O157:H7

Di Zhang[a,b], Haoxin Li[a], Kai Wang[a], Yujian Sun[a], Chenguang Wang[a], Yingying Wang[a], Qiang Bai[a,*], Tianzhi Yu[b], Zhugen Yang[c,*], Ning Sui[a,*], Lina Wang[d,*],

[a] *College of Materials Science and Engineering, Qingdao University of Science and Technology, 53 Zhengzhou Road, Qingdao, Shandong 266042, China*

[b] *Key Laboratory of Opto-Electronic Technology and Intelligent Control (Ministry of Education), Lanzhou Jiaotong University, Lanzhou, 730070, China*

[c] *Faculty of Engineering and Applied Sciences, Cranfield University, Cranfield, MK43 0AL, United Kingdom*

[d] *College of Environment and Safety Engineering, Qingdao University of Science and Technology, 53 Zhengzhou Road, Qingdao, Shandong 266042, China*

[*]Corresponding authors: Q. Bai (baiqiang@qust.edu.cn), Z. Yang (zhugen.yang@cranfield.ac.uk), N. Sui (suining@qust.edu.cn) L. Wang (linawang@qust.edu.cn)

Abstract

In the past two decades, nanozymes have garnered increasing interest, however, their catalytic activity and efficacy still lag significantly behind that of natural enzymes, posing limitations on their utility in bioanalytical applications. In this study, we introduced a novel $BaTiO_3$/graphdiyne/Au (BGA) nanozyme that leverages surface plasmon resonance and piezoelectric effects to concurrently respond to light and ultrasound (US) stimulation, resulting in a 3.8-fold enhancement in peroxidase-like activity. Theoretical and experimental findings suggest that US stimulation induces lattice distortion in $BaTiO_3$, leading to the reversible conversion of C≡C bonds to C=C bonds in graphdiyne. Consequently, the liberated electrons recombine with the hot holes produced by Au nanoparticles upon light excitation, thereby efficiently inhibiting the recombination of hot electron-hole pairs and substantially augmenting peroxidase-like activity. The BGA nanozyme was further configured as a detection platform for *E. coli* O157:H7. The sensor exhibited a broad linear range ($1–10^7$ CFU mL^{-1}) and a low limit of detection of 7 CFU mL^{-1}. Moreover, the sensor exhibited exceptional applicability in the analysis of various real samples such as milk and lemon juice. This study presents a novel research framework for constructing high-activity nanozyme sensors responsive to external fields, offering significant potential in biological analysis, environmental surveillance, and food safety applications.

Keywords: nanozyme, graphdiyne, plasmonic, piezoelectric, colorimetric sensor

Published by Elsevier. This is the Author Accepted Manuscript issued with: Creative Commons Attribution License (CC:BY 4.0).
The final published version (version of record) is available online at DOI:10.1016/j.snb.2025.137378. Please refer to any applicable publisher terms of use.

Introduction

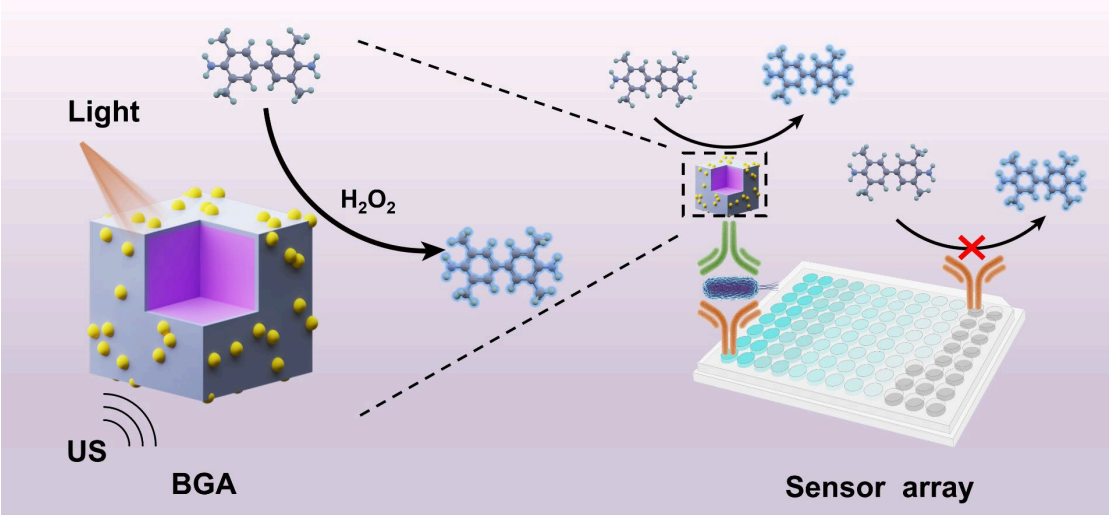
Bacterial pathogens pose a growing threat to global public health, presenting significant challenges. These infections not only result in considerable economic impact but also endanger human health, disrupting normal daily activities. Traditional culture-based methods, while time-consuming, often lack sensitivity. Molecular techniques such as polymerase chain reaction (PCR) have emerged as a gold standard due to their sensitivity and reliability; however, they typically require specialized laboratory facilities and trained personnel[1, 2]. Consequently, the rapid and sensitive detection of bacteria is crucial for safeguarding human health. Various innovative detection methods have been developed at the intersection of biological and engineering sciences[3], encompassing plate culture[4], PCR[5], colorimetric assays[6], electrochemical sensors[7], and surface-enhanced Raman scattering (SERS)[8]. Among these techniques, colorimetric immunoassays stand out for their rapidity, sensitivity, portability, multiplexing capability, and cost-effectiveness[9]. Moreover, they offer non-destructive sample analysis and high throughput, enabling the simultaneous processing of numerous samples to enhance detection efficiency[10-12]. Therefore, the colorimetric immunoassay exhibits excellent reliability and significant potential for the detection of bacterial pathogens.

Nanozymes, nanomaterials that mimic the catalytic activity of natural enzymes, offer distinctive advantages such as superior stability, enhanced activity, cost-effectiveness, and scalability, rendering them highly promising for applications in environmental, biological, and medical domains[13-16]. Nanozymes have garnered considerable attention from researchers due to their exceptional benefits in detection. A wide array of nanozymes, including metal oxides, metal-organic frameworks, noble metals, and carbon nanomaterials, have been identified to exhibit peroxidase (POD)-like activity, serving as nanoprobes for colorimetric detection of various markers[17-22]. Nevertheless, these colorimetric assays frequently encounter issues related to low sensitivity, largely attributed to the limited activity of existing nanozymes[23]. Researchers have investigated diverse strategies to boost nanozyme activity, including morphological, compositional, and surface property modifications, yielding some advancements[24-27]. However, a universally accepted or standard technique for enhancing nanozyme activity has yet to be established, underscoring the critical necessity for a simple and universal approach to regulate and enhance nanozyme

activity.

In recent years, substantial advancements have been achieved in the application of external field-responsive nanozymes for detection purposes. These nanozymes possess catalytic activities that can be precisely regulated by external physical fields, such as light, electricity, or magnetism, thereby significantly enhancing the sensitivity and selectivity of detection techniques. Light, serving as a noninvasive excitation energy source, provides exceptional temporal and spatial resolution, with easily adjustable intensity and wavelength. These attributes position light as a promising avenue for devising a versatile approach to amplify nanozyme activity through light energy utilization. Plasmonic nanostructures, characterized by their extensive tunable absorption spectrum spanning from ultraviolet to infrared wavelengths, facilitate light energy absorption and conversion when integrated with nanozymes[28]. Our previous work has demonstrated that plasmonic nanozymes exhibit the capability to efficiently convert light energy into chemical energy, thereby enhancing nanozyme performance[29-31]. Ultrasound (US) can serve as an external stimulus on piezoelectric materials, inducing the generation of positive and negative charges through the piezoelectric effect, which can impact nanozyme activity[31-33]. The absence of center symmetry in piezoelectric materials results in the production of opposing polarization charges on the material's two surfaces under US exposure. These separated charge carriers can initiate reactions with nearby substances like O_2 and H_2O_2[34, 35], leading to a significant enhancement in nanozyme activity. Our previous investigations have demonstrated the activities of graphdiyne (GDY) nanozyme can be enhanced by a factor of 2-5 under US stimulation[29, 36-38]. Therefore, external field-responsive nanozymes offer significant advantages in the field of biomedical detection and hold great promise for transformative applications in areas such as disease diagnosis and environmental monitoring[39-41]. With the continuous advancement of nanotechnology, the potential applications of these nanozymes are expected to expand even further.

In this work, $BaTiO_3$/graphdiyne/Au (BGA) nano heterojunctions were synthesized for colorimetric detection of bacteria. The lattice distortion of $BaTiO_3$ (BTO) induced by US stimulation led to the reversible conversion of C≡C to C=C in GDY. Consequently, the released electrons recombined with the hot holes generated by Au nanoparticles (AuNPs) upon light excitation, effectively suppressing the recombination of hot electron-hole pairs and significantly enhancing POD-like activity. Building on these results, a colorimetric immunoassay platform for bacterial detection was developed, as depicted in Scheme 1. The BGA demonstrated remarkable sensitivity for colorimetric detection under the combined influence of light and US. Furthermore, a batch colorimetric immunoassay platform was proposed, exhibiting exceptional performance in the detection of real samples.



Scheme 1. Schematic diagram of *E. coli* O157:H7 detection based on external field response.

2. Methods

2.1 Synthesis of BTO

Barium titanate cubes were synthesized via a hydrothermal method. A 70 mL aqueous solution containing $BaCl_2 \cdot 2H_2O$ (0.32 M), TiO_2 (0.2 M), KOH (2.3 M), and PVP (100 g/L) was transferred to a 100 mL PTFE-lined stainless steel autoclave and heated in an oven at 220°C for 24 hours. After the reaction was complete, the precipitate was collected by centrifugation, washed 3 times with deionized water and acetic acid, and then dried under vacuum at 80°C.

2.2 Synthesis of $BaTiO_3$/graphidyne (BTO/GDY)

GDY was synthesized on BTO via a Glaser-Hay coupling reaction, in which hexaethynylbenzene (HEB) was used as the monomer. To initiate the reaction, 10 ml of HEB (7.5 mg) acetone solvent was added dropwise to a three-necked flask containing 50 mL of acetone, 100 mg of BTO and 5 ml of pyridine under argon atmosphere. The reaction mixture was kept at 60°C under argon for 15 hours. Upon completion of the reaction, a thin layer of GDY was applied to the BTO and the product was washed with N, N-dimethylformamide (DMF), ethanol and acetone. Finally, the BTO/GDY complex was freeze-dried.

2.3 Synthesis of BGA

10 mg of BTO/GDY were ultrasonically dispersed for 5 minutes and then mixed with 52 μL of $HAuCl_4 \cdot 4H_2O$ (48.56 mM), followed by stirring. Then, 1 mL of $NaBH_4$ (1 mg mL^{-1}) was added to the above mixture. After reacting 10 minutes, the product was washed 3 times with deionized water and freeze-dried to obtain BGA.

2.4 Colorimetric detection of *E. coli* O157:H7

E. coli suspensions were diluted to various concentrations (10^8, 10^7, 10^6, 10^5, 10^4, 10^3, 10^2, 10 CFU mL^{-1}) using PBS buffer solution. Then, 1.0 mL of the bacterial suspension was added to a cuvette pre-coated with antibody Ab1. After 15 minutes of vigorous shaking on a thermostatic oscillator at 37°C, 150 μL of the BGA-Ab2 probe solution was added and incubated for another 15 minutes. The uncaptured BGA solution was then discarded. Subsequently, a pH 4.0 buffer solution, 1 mM TMB, and 20 mM H_2O_2 were added. The UV-vis absorbance curve was measured using a UV-vis spectrophotometer after 5 minutes of combined light and US treatment. A bacteria-free buffer solution served as a blank control.

For batch testing, optical images of oxTMB were captured with a smartphone. The RGB values of selected areas in the images were extracted using a color recognition app. A linear calibration curve was established between the B/(R+G+B) values and the bacterial concentration, which was then used to compare with the output picture values to determine the *E. coli* concentration.

2.5 Specificity Assay

To evaluate the specificity of BGA for detecting *E. coli* O157:H7, simultaneous detection of *E. coli* and other bacterial strains (*Listeria monocytogenes, Staphylococcus aureus, Vibrio parahaemolyticus, Bacillus cereus, Salmonella typhimurium, and Pseudomonas aeruginosa*) was performed at the same bacterial concentration (10^6 CFU

mL^{-1}). PBS buffer was used as a negative control.

2.6 Detection in actual samples

Fresh lemons and pasteurized milk were purchased from local supermarkets. After a 10-fold dilution with sterile PBS buffer solution, various concentrations of E. coli (10–10^7 CFU mL^{-1}) were added to create spiked samples. These spiked samples were then evaluated under the same conditions as previously described. The recovery rates (%) of *E. coli* in the milk and lemon samples were calculated using the calibration curves obtained earlier.

3. Results and Discussion

Fig. 1a depicts the synthesis pathway of BGA. The TEM images in Fig. 1b exhibit the cubic nanostructure of BGA, with an average diameter of approximately 300 nm. GDY is uniformly coated on the surface of BTO, and AuNPs are evenly dispersed on the BTO/GDY surface (Fig. 1c). The high-resolution transmission electron microscopy (HRTEM) image of BGA (Fig. 1d) reveals lattice spacings of 0.235 nm and 0.405 nm, corresponding to the (111) plane of AuNPs and the (100) plane of BTO[42, 43], respectively, indicating well-crystallized Au and BTO with specific crystalline orientations. Elemental mapping in Fig. 1e illustrates the homogeneous distribution of Ba, Ti, C, O, and Au on the BGA surface. These analyses confirm the successful formation of the BGA heterostructures.

The Raman spectrum of BGA (Fig. 1f) reveals minor peaks at 1912 cm^{-1} and 2103 cm^{-1}, corresponding to the alkyne groups of GDY[44]. Comparative analysis of the Raman spectra indicates that BGA exhibit the characteristic peaks of GDY, along with the retention of BTO characteristic peaks at 276 cm^{-1} and 527 cm^{-1}, confirming the successful synthesis of the BGA heterojunction. The crystal structures of the samples were further examined using X-ray diffraction (XRD). As shown in Fig. 1g, both BTO and BTO/GDY displayed tetragonal crystal structures (PDF#05–0626), with an additional diffraction peak at 38.2° arising after AuNPs incorporation, corresponding to the (111) plane of the face-centered cubic unit cell structure of Au (PDF#65–2870) (Fig. 1g, S2). X-ray photoelectron spectroscopy (XPS) was employed to analyze the chemical states of BGA, with a focus on the C1s peaks (Fig. 1i). The subpeaks observed in the C1s spectrum correspond to C-C (sp^2), C-C (sp), C-O, and C=O, with respective

binding energies of 284.55, 285.0, 286.2, and 288.0 eV[45]. The high-resolution XPS spectra of Ba 3d profiles are presented in Fig. 1j. In the pristine BTO sample, the Ba $3d_{5/2}$ and Ba $3d_{3/2}$ peaks are situated at 779.45 and 794.45 eV, indicative of Ba atoms within the ABO_3 chalcogenide structure[46]. Conversely, in BTO/GDY and BGA samples, the Ba $3d_{5/2}$ and Ba $3d_{3/2}$ peaks exhibit a shift to 779.25 and 794.35 eV, respectively, signifying Ba atoms in a non-calcite structure[47]. Compared to bare BTO, the peak positions observed in BTO/GDY and BGA exhibit a shift towards higher energy values, possibly attributed to surface defects and lattice distortions within the heterostructures. In the XPS spectrum of BGA (Fig. 1k), the two Ti 2p peaks located at 458.4 and 464.2 eV are assigned to the $2p_{3/2}$ and $2p_{1/2}$ peaks of Ti^{4+}[48].

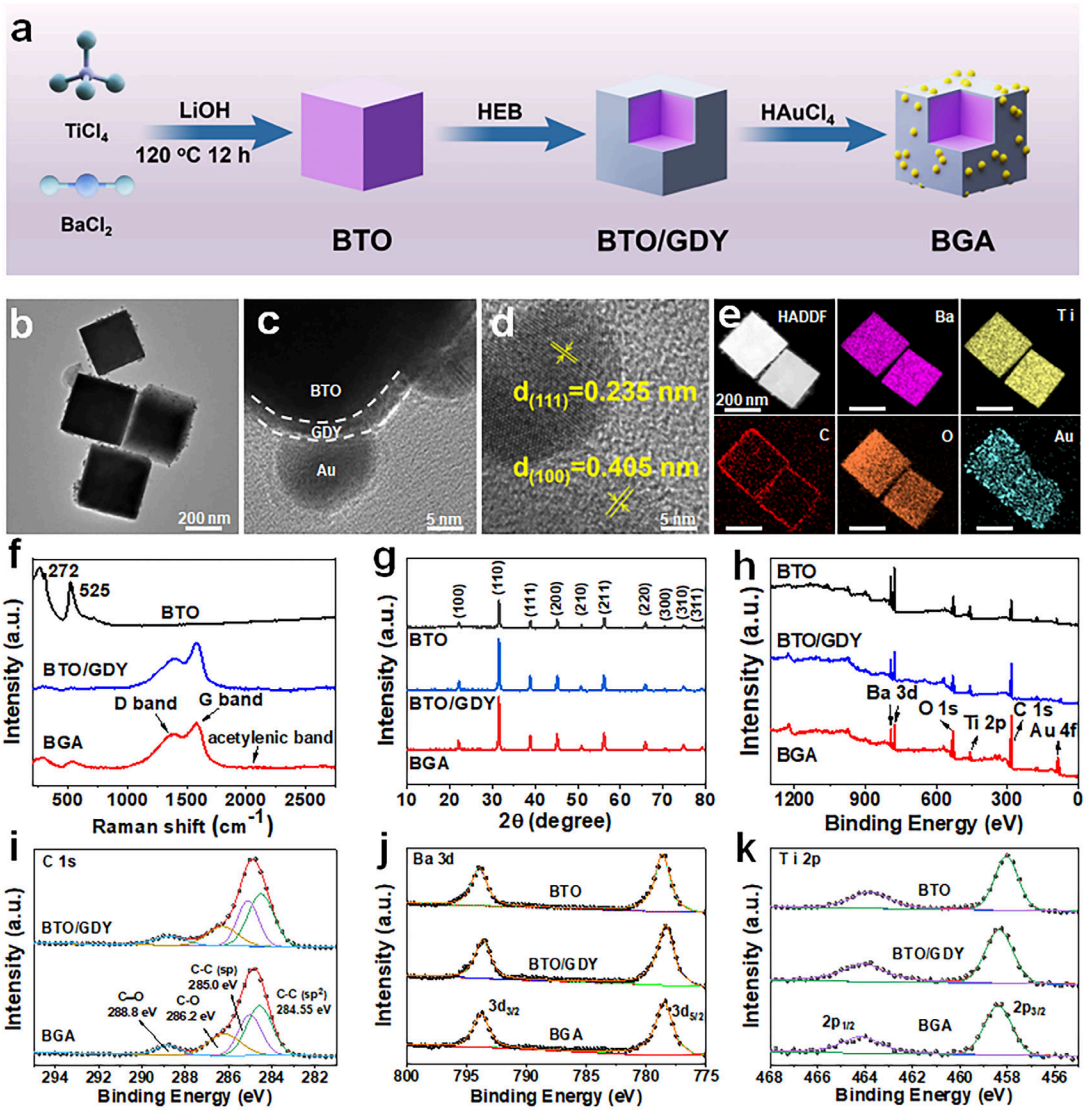


Fig. 1. Synthesis and characterization of BGA (a) Synthetic route, (b) (c) high magnification of TEM and (d) HRTEM images of BGA. (e) TEM image and EDS elemental maps of BGA. (f) Raman spectra of BTO, BTO/GDY, and BGA. (g) XRD patterns of BTO, BTO/GDY, and BGA. (h) XPS

spectra of BTO, BTO/GDY, and BGA, (i) C 1 s, (j) Ba 3d, and (k) Ti 2p.

3.2 Peroxidase-like activity of BGA

To validate the POD-like activity of BGA, TMB was utilized as a model substrate for oxidation, and the absorbance of oxTMB at 652 nm was quantitatively measured to evaluate the POD-like activity of BGA. Fig. 2a illustrates the absorbance variations of BGA under various conditions. No significant UV absorption peaks were detected in the presence of only H_2O_2/TMB or BGA/TMB, indicating the absence of oxTMB generation. In contrast, a visible UV absorption peak at 652 nm was observed when H_2O_2, TMB, and BGA were present simultaneously, confirming the POD-like properties of BGA. Fig. 2b illustrates that the absorbance values of the BGA/TMB/H_2O_2 system were significantly enhanced by the application of light and US stimulation. Specifically, the POD-like activity increased by 2.11-fold with light, 1.44-fold with US, and 3.8-fold with the combined presence of light and US, in comparison to the system without any external fields applied. In Fig. 2c, the relative activity of each material under different external field conditions is depicted, with BGA showcasing the maximum enzyme activity under US/light conditions. (Fig. S3 shows the absorbance curves of each system under different external field conditions).

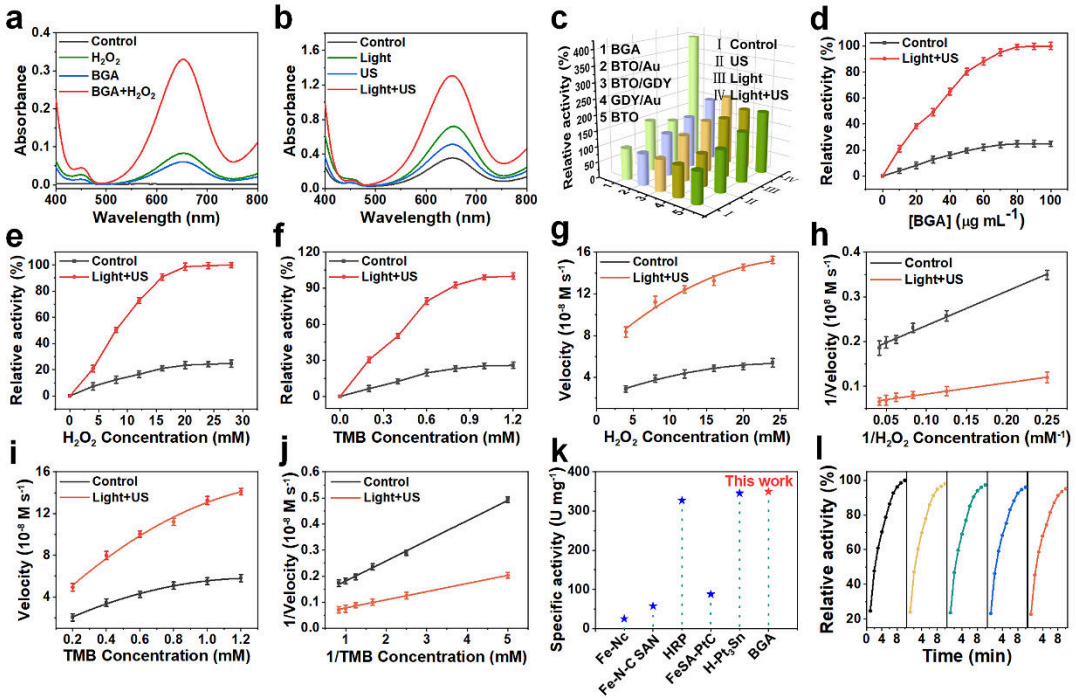


Fig. 2 (a), (b) and (c) Comparison of POD-like activities among various nanozymes. The reaction conditions were 25 °C for 10 min in buffer (pH 4.0). (d), (e) and (f) Comparison of POD-like activities of BGA at various concentration (0–100 μg mL^{-1}), H_2O_2 concentration (0–28 mM) and TMB concentration (0–1.2 mM). (g) Steady-state kinetic assay of BGA with H_2O_2 as substrate. (h) Comparison of H_2O_2 kinetics of BGA under different conditions. (i) Steady-state kinetic assay of BGA with TMB as substrate. (j) Comparison of TMB kinetics of BGA under different conditions. (k) Comparison of the specific activity of POD-like catalytic performance of various nanozymes. (l) 5 cycles of catalytic TMB oxidation rate.

To optimize the reaction conditions for BGA, the concentrations of H_2O_2 and TMB, as well as the pH and temperature, were systematically investigated. Fig. 2d-f illustrate the effects of BGA, H_2O_2, and TMB concentrations on POD-like activity. The absorbance exhibited a gradual increase with higher concentrations of these components, and optimal values were determined to be 100 μg mL^{-1} for BGA, 20 mM for H_2O_2, and 1 mM for TMB. The POD-like activity of BGA demonstrated an initial increase followed by a decrease as pH increased, with the highest activity observed at pH 4.0 (Fig. S4). As depicted in Fig. S5, the POD-like activity increased with temperature, and the activity of BGA remained stable at temperatures exceeding 50 °C, indicating good temperature stability. Since all reactions were conducted at room temperature, subsequent experiments were carried out at 25°C. Fig. S6 illustrates the time-dependent nature of the POD-like activity of BGA; under optimal conditions, the

absorbance at 652 nm in the BGA/TMB/H_2O_2 system increased significantly over time, reaching a plateau after 10 minutes, signifying the catalyst's saturation.

The steady-state kinetics of POD-like activity of BGA were analyzed. The concentration of TMB was maintained at 1 mM, while the concentration of H_2O_2 was varied from 5 to 25 mM. A Michaelis-Menten curve illustrating the reaction rate as a function of substrate concentration was generated (Fig. 2g). From the Lineweaver-Burk plot (Fig. 2h), the maximum initial rate (V_{max}) and Michaelis constant (K_m) were determined to be V_{max} = 18.13x10^{-8} M s^{-1} and K_m = 5.83 mM, respectively. Similarly, in the catalytic reaction of BGA using TMB as the substrate (with H_2O_2 concentration maintained at 20 mM), the reaction also followed the classical Michaelis-Menten model, with V_{max} = 18.29x10^{-8} M s^{-1} and K_m = 0.29 mM (Fig. 2i, j).

Upon exposure to light and US stimulation, the V_{max} values for H_2O_2 and TMB increased by 3.2 and 2.7 times, respectively, compared to those in the absence of external fields (Table S1, Fig. 2h, j). The kinetic fitting curve of BGA under individual external field conditions is presented in Fig. S7, providing additional evidence that light and US can augment the POD-like activity of BGA. The K_m value is indicative of the enzyme's substrate affinity, where lower values signify higher affinity[49]. A comparison of the kinetic parameters of BGA and natural horseradish peroxidase (HRP) (Table S1) revealed that the K_m value of BGA for TMB was lower than that of HRP, suggesting that BGA exhibits a stronger affinity for TMB substrates. The observed increase in the K_m of BGA for H_2O_2 under light irradiation compared to dark conditions suggests a reduced affinity of BGA for H_2O_2 in the presence of light. This phenomenon can likely be attributed to the rapid decomposition of H_2O_2 on the BGA surface under light irradiation, which depletes the local substrate concentration near the active sites, thereby reducing the apparent affinity. Furthermore, K_m reflects the substrate concentration at which the reaction rate reaches half of its maximum value. Under the combined effects of US and light irradiation, the activity of BGA nanozyme activity was significantly enhanced, as evidenced by the smallest K_m value observed, indicating an improved affinity for H_2O_2. These results demonstrate that external field stimulation effectively enhances the activity of BGA nanozyme, providing further validation of its catalytic performance. Furthermore, the affinity and maximum reaction rate (V_{max}) of

BGA towards H_2O_2 and TMB surpassed those of most other nanozymes. Under optimal conditions, the maximum specific activity of BGA was determined to be 379.48 U mg^{-1} (Fig. 2k), and BGA also demonstrated remarkably high POD-like activity in comparison to other reported nanozymes[50-53]. The catalytic activity and stability of BGA were further assessed through TMB oxidation cycle experiments. As depicted in Fig. 2l, the normalized POD-like activity of BGA remained at approximately 95% after five cycles of US and light treatment, underscoring the excellent catalytic stability and durability of BGA nanozymes. Furthermore, characterization experiments conducted on the post-reaction BGA further confirmed this conclusion (Fig. S8).

3.3 Catalytic mechanism

Reactive oxygen species (ROS) are typically regarded as active intermediates that promote POD-like catalytic reactions. In order to explore the involvement of ROS in the catalytic activity, a series of burst experiments were conducted. Prior investigations have indicated that ROS typically include hydroxyl radical (•OH), singlet oxygen ($^1O_2$) and superoxide radical ($•O_2^-$) [54]. To confirm the impact of ROS in the H_2O_2-catalyzed oxidation of TMB by BGA nanozyme, three free radical scavengers were employed: 1,4-benzoquinone (BQ) to capture $•O_2^-$, isopropanol (IPA) for •OH, and L-histidine (His) for $^1O_2$. The findings demonstrated an 83.1% decrease in POD-like activity when •OH was sequestered by IPA. Conversely, the presence of BQ and His resulted in an 9.5% and 8.9% decline in enzyme activity, respectively. This suggests that although all three ROS ($•O_2^-$, •OH, and $^1O_2$) were produced during the catalytic process, •OH exerted the most substantial influence (Fig. S9).

To further validate these findings, we employed electron paramagnetic resonance (EPR) spectroscopy in conjunction with spin trapping techniques to detect the presence of ROS. By utilizing DMPO and TEMP as spin traps for hydroxyl radicals, superoxide and singlet oxygen[55, 56], we identified the formation of DMPO-•OH adducts in the presence of hydroxyl radicals, which exhibited a 1:2:2:1 quadruple EPR signal pattern. When the BGA nanozyme was incubated with DMPO and H_2O_2, no significant EPR

peaks were detected, suggesting minimal or no •OH production. However, upon the application of an external electric field, a distinct quadruple signal peak with an intensity ratio of 1:2:2:1 emerged, indicating the generation of •OH (Fig. 3a). The EPR signal intensity notably increased when both light and US were concurrently applied, suggesting that the BGA nanozyme more efficiently converted H_2O_2 to •OH under the combined effect of light and US, suggesting a synergistic effect of light and US in promoting free radical generation.

Fig. 3a also shows the characteristic TEMP-$^1O_2$ (1:1:1) and DMPO-•O_2^- (1:1:1:1) peaks, providing evidence for the production of singlet oxygen ($^1O_2$) and superoxide radicals (•O_2^-). Given that the catalytic efficiency of BGA nanozyme was optimized at pH 4.0, it can be inferred that the active site of BGA facilitates the reduction of H_2O_2 to •OH, $^1O_2$, and •O_2^- followed by the oxidation of TMB to the chromogenic product oxTMB under acidic conditions rich in H^+ ions.

The photocurrent response and piezoelectric characteristics of the materials were evaluated, demonstrating that BGA displays enhanced conductivity and improved interfacial charge carrier transfer efficiency (Fig. S10). Additionally, the BGA heterostructures exhibit outstanding piezoelectric properties, as outlined in Fig. S11.

Fig. S12 illustrates the atomic model of BGA, including the calculated lattice constants, energies, and structural correspondences for GDY and BTO. GDY exhibits stability within a range of 7.09-10.40 Å (Fig. S12a); outside this range, its chemical bonds break, hindering its return to a stable state. On the contrary, BTO remains stable within a range of 2.60-4.41 Å, with energy fluctuation differences of approximately 152.60 eV (Fig. S12b). The most stable configurations of GDY and BTO were then used for layer stacking, and their electron density difference (EDD) was calculated. As depicted in Fig. 3b, S13, the electron density difference reveals electron enrichment at the interface between GDY and BTO, accompanied by the creation of multiple holes in the outer layer of BTO. These holes serve as active sites for catalytic reactions at the

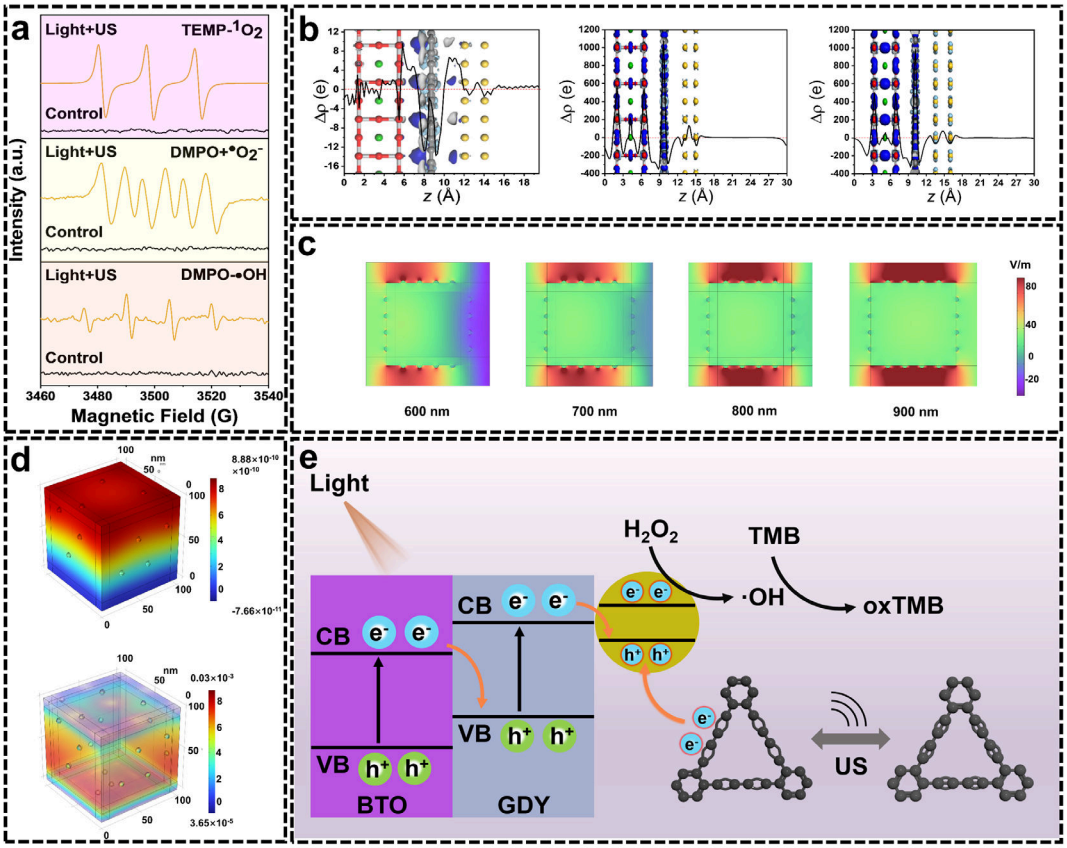


Fig. 3. (a) EPR spectra of TEMP-$^1O_2$ adducts, DMPO-•O_2^-, and DMPO-•OH adducts. [DMPO]=[TEMP]=50 mM. (b) Electron density difference plots for BGA and z-axis values of electron density difference and electron density difference plots of BGA in stretching (left) or compression (right), where positive and negative values represent electron gains and losses. (c) Surface electric field distribution of BGA under different wavelengths of light. (d) Electric field diagram and Electric field diagram of BGA in z-axis US field of BGA. (e) Charge transfer pathways of BGA under light and US and their possible catalytic mechanisms.

vacancies present on the surface of BTO. While augmenting the Au atomic layer has minimal impact on the distribution of the electron cloud between GDY and BTO, it results in an increase in the quantity of electrons and holes on the GDY side, distanced from BTO. This observation implies that GDY has the ability to absorb surplus electrons from BTO within the lattice range of approximately 8.5-10 Å along the z-axis (Fig. 3b). Under the influence of US, the lattice constants of GDY and BTO undergo fluctuations, causing them to deviate from the state of minimum energy. This necessitates the utilization of internal energy to restore them to a stable condition. The electric field strengths at various wavelengths (Fig. 3c, S14) illuminating diverse regions of BGA were computed. Irrespective of the wavelength, the surface of AuNPs

and the aqueous medium exhibited a more intense positive electric field compared to BTO and GDY, thereby attracting electrons toward the surface of AuNPs. When subjected to light with a wavelength of 600 nm, BGA displayed a negative electric field at the GDY, facilitating the transfer of electrons from GDY to the AuNPs. The simulated temperature variation of BGA under light exposure in an aqueous environment (Fig. S15) revealed a slightly elevated temperature at the material's surface in comparison to its interior; nevertheless, the overall temperature change was negligible, suggesting that the photothermal effect does not exert a predominant influence on the catalytic process.

Furthermore, the application of mechanical force on BGA results in the experience of varying stress magnitudes at distinct locations, causing deformation and inducing polarization. As depicted in Fig. 3d, the surface potential distribution of BGA under mechanical forces illustrates the migration of electrons from regions of low potential to those of high potential during the catalytic reaction. When BGA is subjected to mechanical force, the surface potential of AuNPs surpasses that of GDY, indicating the transfer of electrons from GDY to AuNPs. In the interaction between BTO and GDY, forming a Z-type heterojunction, electrons flow from BTO to GDY. Owing to the disparity in Fermi energy levels between GDY and AuNPs, charge carriers are redistributed across the interface, leading to electron transfer from GDY to AuNPs. Under light exposure, BGA initiates the generation of electron-hole pairs in the valence band (VB) of BTO and the conduction band (CB) of GDY. Electrons originating from the CB of BTO migrate to the VB of GDY, where they engage in recombination with holes. Simultaneously, the positive charge present on BTO facilitates the reduction of OH- to -OH (Fig. 3e). Through the localized surface plasmon resonance (LSPR) effect, gold generates a substantial number of hot electron-hole pairs when subjected to light irradiation. The variation in Fermi energy levels prompts electrons from GDY to transfer to the gold surface, where they combine with hot holes. Consequently, AuNPs act as active sites for catalyzing the decomposition of H_2O_2, thereby augmenting the catalytic performance of BGA. GDY is rich in C≡C bonds, which, upon exposure to US, undergo conversion to C=C bonds, liberating electrons that further enhance the catalytic efficiency. Under US stimulation, BGA undergoes mechanical vibrations causing the stretching of Ti-O bonds in BTO. This elongation results in a decrease in the electron cloud density, creating additional holes that facilitate the reduction of OH-

to -OH. Concurrently, the conversion of C≡C bonds in GDY to C=C bonds occur, leading to an expansion in the overall lattice constant and the formation of holes capable of accepting electrons from BTO. Conversely, when the Ti-O bonds in BTO are compressed by US, the electron cloud density surrounding BTO increases, prompting the transfer of electrons to GDY. This compression also induces the transformation of C≡C bonds in GDY to C=C bonds, reducing the total lattice constant and generating surplus electrons that elevate the electron cloud density around the AuNPs. When exposed to light irradiation, electrons on the gold surface experience enhanced excitation, generating hot electrons that facilitate the decomposition of H_2O_2.

4. Detection of *E.coli* and practical application

Capitalizing on the exceptional POD-like activity of BGA in response to external stimuli, a sensor for detecting *E. coli* was devised, as depicted in Fig. 4a. *E. coli* was immobilized in a 96-well plate using the Ab1 antibody, following which a BGA bioprobe modified with the Ab2 antibody was introduced. The Ab2 antibody spontaneously binds to *E. coli*, immobilizing the BGA probe in the 96-well plate, thereby showcasing remarkable POD-like enzyme performance under the influence of light and US. The alteration in absorbance of oxTMB was tracked at 652 nm (the peak absorbance of oxTMB) to evaluate the sensitivity of the BGA nanozyme to *E. coli* CFUs (Fig. 4b)[57]. The UV absorption intensity at 652 nm exhibited a gradual increase with escalating bacterial concentrations, ranging from 10^1 CFU mL^{-1} to 10^8 CFU mL^{-1}. Fig. 4c illustrates a robust linear correlation between the change in oxTMB absorbance ($\Delta A = A-A_0$, where A represents the absorbance at the specific concentration and A_0 denotes the absorbance in the negative control group) and the *E. coli* concentration (x) within the interval of 10^1 CFU mL^{-1} to 10^8 CFU mL^{-1}, presented as $y = 0.02x - 0.05$ (x = log(*E. coli* concentration)) with an R^2 value of 0.988. The lower limit of detection (LOD) was established at 7 CFU mL^{-1} (3σ)[58], which is lower than previous values (Table S3). Furthermore, to validate the specificity of the sensor in detecting *E. coli*, experiments were conducted using *E. coli* and other bacterial strains (*Listeria monocytogenes, Staphylococcus aureus, Vibrio parahaemolyticus, Bacillus cereus, Salmonella typhimurium, and Pseudomonas aeruginosa*) at an equivalent concentration (10^6 CFU/mL). PBS was utilized as a negative control. As depicted in Fig. 4d, solely the *E. coli* group exhibited notable variations in the oxTMB absorbance curve, confirming the

sensor's specificity for *E. coli* detection.

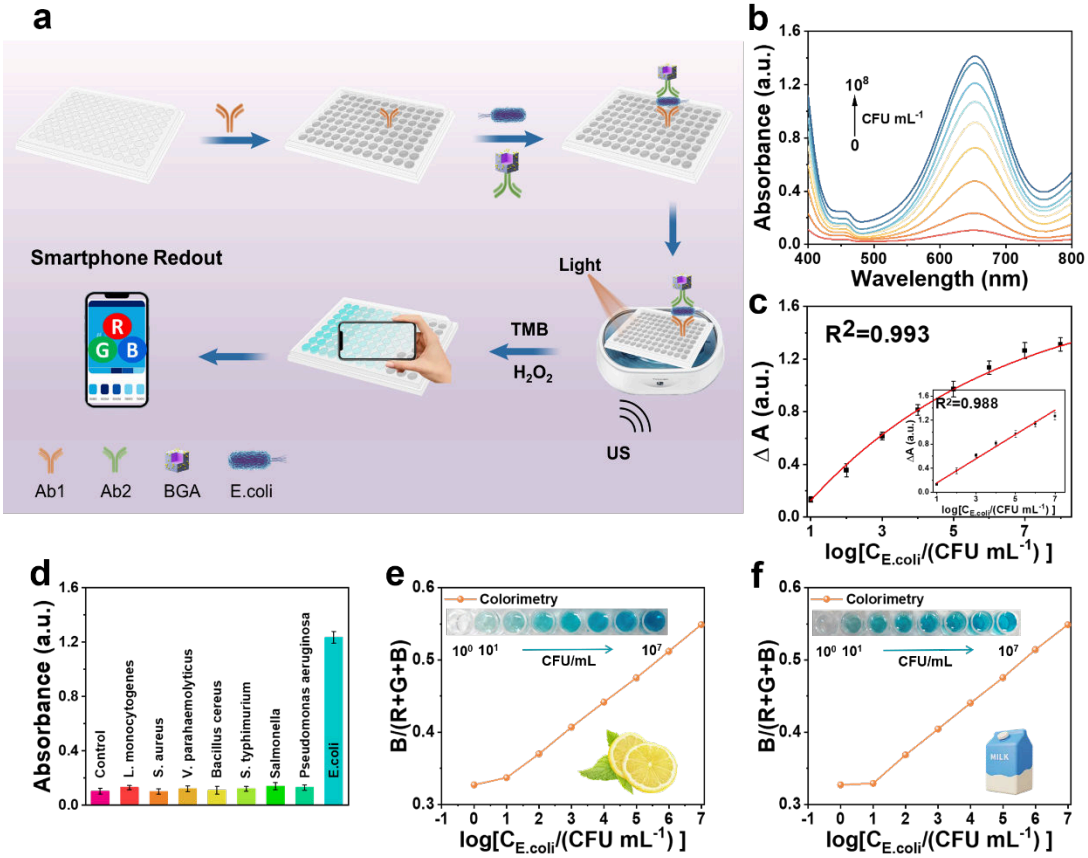


Fig. 4 Detection of *E. coli*. (a) Schematic diagram of portable quickly detection. (b) UV-visible absorption spectra of BGA-catalyzed TMB oxidation under different bacterial concentration conditions. (c) Linear relationship between the change in absorbance of oxTMB and bacterial concentration. Specificity of the detection platform for different bacteria (d) Specificity of the detection platform for *E. coli*. Relationship between B/(R + G + B) ratio and *E. coli* concentration of the actual sample assay. (e) Lemon (f) Milk. The inset shows the oxTMB color development results corresponding to each bacterial concentration.

To assess the applicability of the colorimetric sensor in analyzing real-world samples, milk and lemon juice were chosen as spiked samples. The testing methodology is elucidated in Fig. 4a. The color development resulting from the catalytic action on TMB was monitored, and the RGB values of each colored region were quantified. Through a comparison of these values with the standard curve (Fig. S16), rapid and straightforward batch detection of *E. coli* can be accomplished. The outcomes are delineated in Fig. 4e, f, where the B/(R+B+G) values exhibited a positive correlation with the *E. coli* concentration. The LOD was determined to be 10 CFU mL^{-1} for lemon juice and 10^2 CFU mL^{-1} for milk. The higher detection threshold in milk is attributed

to the presence of proteins and other substances that are challenging to segregate via high-speed centrifugation, thereby impeding the adsorption capacity of the BGA signal probe and resulting in lower concentrations than anticipated from colorimetric detection in real samples. Moreover, recovery experiments were conducted to validate the accuracy and precision of the outcomes, with average *E. coli* recoveries in the samples falling within the range of 89.0% to 112.6%, accompanied by an RSD not exceeding 8.9% (Table 1). These results underscore the dependability of our sensor in detecting *E. coli* O157 in food samples, highlighting its promising prospects for practical applications.

Table 1 Peak recoveries of *E. coli* in real samples tested by BGA

Sample	Add *E.coli* (CFU mL^{-1})	Find *E.coli* (CFU mL^{-1})	Recovery (%)	RSD (%)
lemon 1	10^1	11	110.0	3.2
lemon 2	10^2	97	97.0	3.6
lemon 3	10^3	1071	107.1	2.3
lemon 4	10^4	10209	102.1	1.3
lemon 5	10^5	90420	90.4	3.3
lemon 6	10^6	980728	98.1	4.3
lemon 7	10^7	10715193	107.2	7.4
milk 1	10^1	-	-	-
milk 2	10^2	89	89.0	3.5
milk 3	10^3	910	91.0	4.3
milk 4	10^4	9426	94.2	4.7
milk 5	10^5	91676	91.6	5.7
milk 6	10^6	1092018	109.2	4.7
milk 7	10^7	11265961	112.6	8.9

Conclusion

In this study, we synthesized a heterostructure comprising a BGA nanozyme displaying POD-like activity. This nanozyme showcased sensitivity to both light and US, manifesting a 3.8-fold amplification in POD-like activity upon concurrent exposure to light and US stimulation. This augmentation can be ascribed to the lattice distortion of BTO prompted by US stimulation, instigating the reversible transformation of C≡C

bonds to C=C bonds in GDY. Consequently, the liberated electrons combine with the hot holes generated by AuNPs under light excitation, effectively inhibiting the recombination of hot electron-hole pairs and notably enhancing the POD-like activity. This photo/piezoresponsive nanozyme was devised as a framework for *E. coli* detection. The sensor showcased an extensive linear range (1–10^7 CFU mL^{-1}) and a low LOD of 7 CFU mL^{-1}. Assessments conducted on authentic samples (milk, lemon juice) underscore the potential of this innovative platform for diverse applications in environmental and food analysis, as well as in biological analysis.

Declaration of Competing Interest

The authors declare no conflicts of interest.

Acknowledgements

This work was supported by the National Natural Science Foundation of China (Grant No. 22375112), Natural Science Foundation of Shandong Province (Grant No. ZR2021MB111, ZR2020MB026, ZR2023ME076).

Reference

[1] L. Cao, X. Cui, J. Hu, Z. Li, J.R. Choi, Q. Yang, M. Lin, L. Ying Hui, F. Xu, Advances in digital polymerase chain reaction (dpcr) and its emerging biomedical applications, Biosens Bioelectron. 90 (2017), pp. 459-474. https://doi.org/10.1016/j.bios.2016.09.082.

[2] A. Gopal, L. Yan, S. Kashif, T. Munshi, V.A.L. Roy, N.H. Voelcker, X. Chen, Biosensors and point-of-care devices for bacterial detection: rapid diagnostics informing antibiotic therapy, Adv. Healthc. 11 (2022), pp. 2101546. https://doi.org/10.1002/adhm.202101546.

[3] C. Spatola Rossi, F. Coulon, S. Ma, Y.S. Zhang, Z. Yang, Microfluidics for rapid detection of live pathogens,Adv. Funct. Mater. 33 (2023), pp. 2212081. https://doi.org/10.1002/adfm.202212081.

[4] S. Yan, Q. Liu, K. Xing, Z. Liu, H. Guo, W. Jiang, X. Ma, M. Yan, C. Wang, X. Liu, D. Xing, Versatile filter membrane for effective sampling and real-time quantitative detection of airborne pathogens,J. Hazard. Mater. 474 (2024), pp. 134740. https://doi.org/10.1016/j.jhazmat.2024.134740.

[5] R. Shen, W. Hui, W. Wu, N. Yang, X. Lin, P.-I. Mak, R.P. Martins, A. Liu, Y. Jia, A cost-effective and field-deployable sensing system for chip-integrated detection of bacteria with the naked eye, Sensor Actuat. B Chem. 410 (2024), pp. 135668. https://doi.org/10.1016/j.snb.2024.135668.

[6] Y. Zhang, M.A. Khan, Z. Yu, W. Yang, H. Zhao, D. Ye, X. Chen, J. Zhang, The identification of oral cariogenic bacteria through colorimetric sensor array based on single-atom nanozymes, Small. 20 (2024), pp. 2403878. https://doi.org/10.1002/smll.202403878.

[7] D. Gunasekaran, I. Rostovsky, D. Taussig, T. Bar-Am, Y. Wine, N. Sal-Man, S. Vernick, A dual-channel electrochemical biosensor enables concurrent detection of pathogens and antibiotic resistance, Biosens Bioelectron. 257 (2024), pp. 116314. https://doi.org/10.1016/j.bios.2024.116314.

[8] J. Li, W. Shen, X. Liang, S. Zheng, Q. Yu, C. Wang, C. Wang, B. Gu, 2D film-like magnetic sers tag with enhanced capture and detection abilities for immunochromatographic diagnosis of multiple bacteria, Small. 20 (2024), pp. 2310014. https://doi.org/10.1002/smll.202310014.

[9] J. Xia, Z. Li, Y. Ding, L.A. Shah, H. Zhao, D. Ye, J. Zhang, Construction and application of nanozyme sensor arrays, Anal. Chem. 96 (2024), pp.8221-8233. https://doi.org/10.1021/acs.analchem.4c00670.

[10] Z. Jin, W. Yim, M. Retout, E. Housel, W. Zhong, J. Zhou, M.S. Strano, J.V. Jokerst, Colorimetric sensing for translational applications: from colorants to mechanisms, Chem. Soc. Rev. 53 (2024), pp. 7681-7741. https://doi.org/10.1039/D4CS00328D.

[11] L. Yang, X. Xu, Y. Song, J. Huang, H. Xu, Research progress of nanozymes in colorimetric biosensing: classification, activity and application, Chem. Eng. J. 487 (2024), pp. 150612. https://doi.org/10.1016/j.cej.2024.150612.

[12] B. Gao, Q. Ye, Y. Ding, Y. Wu, X. Zhao, M. Deng, J. Zhang, M. Chen, Y. Zhang, X. Wei, L. Cao, N. Ling, Y. Ye, Q. Wu, Metal-based nanomaterials with enzyme-like characteristics for bacterial rapid detection and control, Coord. Chem. Rev. 510 (2024), pp. 215799. https://doi.org/10.1016/j.ccr.2024.215799.

[13] L. Gao, J. Zhuang, L. Nie, J. Zhang, Y. Zhang, N. Gu, T. Wang, J. Feng, D. Yang, S. Perrett, X. Yan, Intrinsic peroxidase-like activity of ferromagnetic nanoparticles, Nat. Nanotechnol. 2 (2007), pp.577-583. https://doi.org/10.1038/nnano.2007.260.

[14] H. Wei, E. Wang, Nanomaterials with enzyme-like characteristics (nanozymes):

next-generation artificial enzymes, Chem. Soc. Rev. 42 (2013), pp. 6060-6093. https://doi.org/10.1039/C3CS35486E.
[15] Y. Sun, C. Wang, H. Li, K. Wang, Q. Bai, G. Zhang, et al., sp Carbon Disrupting Axial Symmetry of Local Electric Field for Biomimetic Co nstruction of Three-
Dimensional Geometric and Electronic Structure in Nanozyme, Angew. Chem. Int. Ed., 2024, e202418707. https://doi.org/10.1002/anie.202418707.
[16] F. Ge, Y. Gao, Y. Jiang, Y. Yu, Q. Bai, Y. Liu, et al., Design and performance analysis of multi-enzyme activity-doped nanozymes assisted by machine learning, Colloids and Surfaces B, 248(2025), 114468. https://doi.org/10.1016/j.colsurfb.2024.114468
[17] C. Song, F. Wang, X. Zhang, Y. Ma, Y. Wu, M. He, X. Niu, M. Sun, $CoMnO_x$ nanoflower-based smartphone sensing platform and virtual reality display for colorimetric detection of ziram and Cu^{2+}, Biosensors., 14(4)(2024), pp. 178. https://doi.org/10.3390/bios14040178.
[18] J. Xiao, F. Shi, Y. Zhang, M. Peng, J. Xu, J. Li, Z. Chen, Z. Yang, A MOF nanozyme-mediated acetylcholinesterase-free colorimetric strategy for direct detection of organophosphorus pesticides, Chem. Commun. 60 (2024), pp. 996-999. https://doi.org/10.1039/D3CC05381D.
[19] S. Li, L. Liang, L. Tian, J. Wu, Y. Zhu, Y. Qin, S. Zhao, F. Ye, Enhanced peroxidase-like activity of MOF nanozymes by co-catalysis for colorimetric detection of cholesterol, J. Mater. Chem. B. 11 (2023), pp. 7913-7919. https://doi.org/10.1039/D3TB00958K.
[20] F. Ge, Y. Sun, K. Wang, G. Ma, F. Li, Q. Bai, Y. Liu, N. Sui, Colorimetric/electrochemical dual mode detection ascorbic acid based Au@PdNi nanozyme, Microchem. J. 201 (2024), pp. 110745. https://doi.org/10.1016/j.microc.2024.110745.
[21] Z. Lang, R. Li, R. Javed, H. Zhao, H. Cao, D. Ye, Smartphone-based colorimetric sensor using Fe-N-P-C single-atom nanozymes with boosted activity for sensitive detection of S^{2-}, Microchem. J. 198 (2024), pp. 110169. https://doi.org/10.1016/j.microc.2024.110169.
[22] T. Wang, Q. Bai, Z. Zhu, H. Xiao, F. Jiang, F. Du, W.W. Yu, M. Liu, N. Sui, Graphdiyne-supported palladium-iron nanosheets: A dual-functional peroxidase mimetic nanozyme for glutathione detection and antibacterial application, Chem. Eng. J. 413 (2021), pp. 127537. https://doi.org/10.1016/j.cej.2020.127537.
[23] I. Zare, D. Choi, J. Zhang, M.T. Yaraki, A. Ghaee, S.Z. Nasab, R. Taheri-Ledari, A. Maleki, A. Rahi, K. Fan, J. Lee, Modulating the catalytic activities of nanozymes for molecular sensing, Nano Today. 56 (2024), pp. 102276. https://doi.org/10.1016/j.nantod.2024.102276.
[24] B. Liu, J. Liu, Surface modification of nanozymes, Nano Res. 10 (2017), pp. 1125-1148. https://doi.org/10.1007/s12274-017-1426-5.
[25] Y. Wen, W. Chen, R. Wu, J. Guo, X. Liu, B. Shi, C. Zhang, L. Wu, Y. Zheng, A. Liu, L. Lin, Chitosan-stabilized PtAu nanoparticles with multienzyme-like activity for mixed bacteria infection wound healing and insights into its antibacterial mechanism, Small Struct. 5 (2024), pp. 2300553. https://doi.org/10.1002/sstr.202300553.
[26] P. Zhou, Y. Dai, X. Lin, Y. Song, Y. Pang, R. Chen, R. Xiao, Specific and magnetic covalent organic framework confined Os nanoclusterzyme for interference-free and ultrasensitive biosensing, Adv. Funct. Mater. n/a (2024), pp. 2400875.

https://doi.org/10.1002/adfm.202400875.
[27] F. Jiao, Z. Cai, A smartphone-based nanoenzyme-modulated aptasensor using an infrared camera for rapid detection of kanamycin, Chem. Eng. J. 481 (2024), pp. 148699. https://doi.org/10.1016/j.cej.2024.148699.
[28] G. Xu, X. Du, W. Wang, Y. Qu, X. Liu, M. Zhao, W. Li, Y.-Q. Li, Plasmonic nanozymes: leveraging localized surface plasmon resonance to boost the enzyme-mimicking activity of nanomaterials, Small. 18 (2022), pp. 2204131. https://doi.org/10.1002/smll.202204131.
[29] S. Shi, Y. Jiang, Y. Yu, M. Liang, Q. Bai, L. Wang, D. Yang, N. Sui, Z. Zhu, Piezo-augmented and photocatalytic nanozyme integrated microneedles for antibacterial and anti-inflammatory combination therapy, Adv. Funct. Mater. 33 (2023), pp. 2210850. https://doi.org/10.1002/adfm.202210850.
[30] Z. Zhu, H. Luo, T. Wang, C. Zhang, M. Liang, D. Yang, M. Liu, W.W. Yu, Q. Bai, L. Wang, N. Sui, Plasmon-enhanced peroxidase-like activity of nitrogen-doped graphdiyne oxide quantum dots/gold–silver nanocage heterostructures for antimicrobial applications, Chem. Mater. 34 (2022), pp. 1356-1368. https://doi.org/10.1021/acs.chemmater.1c03952.
[31] W. Feng, Y. Jiang, F. Ge, Q. Bai, J. Yang, L. Shang, R. Cao, G. Niu, L. Wang, Z. Zhu, N. Sui, Interconversion of sp-hybridized chemical bonds induces piezoelectric enhanced photocatalysis, Appl. Catal. B-Environ. 349 (2024), pp. 123868. https://doi.org/10.1016/j.apcatb.2024.123868.
[32] X. Yu, L. Wang, Z. Zhu, X. Han, J. Zhang, A. Wang, L. Ding, J. Liu, Piezoelectric effect modulates nanozyme activity: underlying mechanism and practical application, Small. 19 (2023), pp. 2304818. https://doi.org/10.1002/smll.202304818.
[33] Z. Liu, X. Yu, L. Li, Piezopotential augmented photo- and photoelectro-catalysis with a built-in electric field, Chin. J. Catal. 41 (2020), pp. 534-549. https://doi.org/10.1016/S1872-2067(19)63431-5.
[34] S. Li, M. Yang, Y. Wang, B. Tian, L. Wu, D. Yang, S. Gai, P. Yang, Bridging OER Electrocatalysis and Tumor Therapy: Utilizing piezoelectric-hole-induced OER electrocatalysis for direct oxygen generation to address hypoxia, Adv. Funct. Mater. 34 (2024), pp. 2404169. https://doi.org/10.1002/adfm.202404169.
[35] L. Cai, J. Du, F. Han, T. Shi, H. Zhang, Y. Lu, S. Long, W. Sun, J. Fan, X. Peng, Piezoelectric metal–organic frameworks based sonosensitizer for enhanced nanozyme catalytic and sonodynamic therapies, ACS Nano. 17 (2023), pp. 7901-7910. https://doi.org/10.1021/acsnano.3c01856.
[36] J. Zhang, Q. Bai, X. Bi, C. Zhang, M. Shi, W.W. Yu, F. Du, L. Wang, Z. Wang, Z. Zhu, N. Sui, Piezoelectric enhanced peroxidase-like activity of metal-free sulfur doped graphdiyne nanosheets for efficient water pollutant degradation and bacterial disinfection, Nano Today. 43 (2022), pp. 101429. https://doi.org/10.1016/j.nantod.2022.101429.
[37] Q. Bai, J. Zhang, Y. Yu, C. Zhang, Y. Jiang, D. Yang, M. Liu, L. Wang, F. Du, N. Sui, Z. Zhu, Piezoelectric activatable nanozyme-based skin patch for rapid wound disinfection, ACS Appl. Mater. 14 (2022), pp. 26455-26468. https://doi.org/10.1021/acsami.2c05114.
[38] M. Liang, L. Shang, Y. Yu, Y. Jiang, Q. Bai, J. Ma, D. Yang, N. Sui, Z. Zhu, Ultrasound activatable microneedles for bilaterally augmented sono-chemodynamic and sonothermal antibacterial therapy, Acta Biomater. 158 (2023), pp. 811-826. https://doi.org/10.1016/j.actbio.2022.12.041.

[39] D. Glikman, L. Wyszynski, V. Lindfeld, S. Hochstädt, M.R. Hansen, J. Neugebauer, et al., Charge regulation at the nanoscale as evidenced from light-responsive nanoemulsions, J. Am. Chem. Soc., 146(2024), 8362-71. https:/doi.org/10.1021/jacs.3c14112.
[40] Y. Ma, M. Yu, Z. Sun, S. Pan, Y. Wang, F. Li, X. Guo, R. Zhao, Y. Xu,X. Wu, Biomass-Based, Dual enzyme-responsive nanopesticides: eco-friendly and efficient control of pine wood nematode disease, ACS Nano, 18(2024) 13781-93. https://doi.org/10.1021/acsnano.4c02031.
[41] M. Fu, P. Zhou, W. Sheng, Z. Bai, J. Wang, X. Zhu, L. Hua, B. Pan, F. Gao, Magnetically controlled photothermal, colorimetric, and fluorescence trimode assay for gastric cancer exosomes based on acid-induced decomposition of CP/Mn-PBA DSNBs, Anal. Chem., 96(2024) 4213-23. https://doi.org/10.1021/acs.analchem.3c05550.
[42] J. Wang, X. Qiu, K. Su, S. Wang, J. Li, Y. Tang, Breaking the lattice match of Pd on Au(111) nanowires: manipulating the island and epitaxial growth pathways to boost the oxygen reduction reactivity, J. Mater. Chem. A. 8 (2020), pp. 19300-19308. https://doi.org/10.1039/D0TA05867J.
[43] Z. Zhao, G. Li, Z. Wang, M. Feng, M. Sun, X. Xue, R. Liu, H. Jia, Z. Wang, W. Zhang, H. Li, Z. Chen, Black $BaTiO_3$ as multifunctional sulfur immobilizer for superior lithium sulfur batteries, J. Power Sources. 434 (2019), pp. 226729. https://doi.org/10.1016/j.jpowsour.2019.226729.
[44] X. Luan, L. Qi, Z. Zheng, S. Zhao, H. Liu, R. Liu, Z. Chen, J. Yan, Y. Xue, Y. Li, Controllable growth of WO_3@GDY heterointerface for efficient NH_3 synthesis, Mater. Chem. Front. 7 (2023), pp. 5898-5904. https://doi.org/10.1039/D3QM00734K.
[45] X. Chen, X. Zheng, C. Zhang, D. Zhang, Y. Gao, S. Chen, Y. Xue, Y. Li, Highly selective conversion of CO_2 to formate on SnO_x/GDY heterostructured electrocatalyst, Nano Energy. 114 (2023), pp. 108622. https://doi.org/10.1016/j.nanoen.2023.108622.
[46] H. Zheng, X. Li, K. Zhu, P. Liang, M. Wu, Y. Rao, R. Jian, F. Shi, J. Wang, K. Yan, J. Liu, Semiconducting $BaTiO_3$@C core-shell structure for improving piezo-photocatalytic performance, Nano Energy. 93 (2022), pp. 106831. https://doi.org/10.1016/j.nanoen.2021.106831.
[47] X. Zhou, S. Wu, C. Li, F. Yan, H. Bai, B. Shen, H. Zeng, J. Zhai, Piezophototronic effect in enhancing charge carrier separation and transfer in ZnO/$BaTiO_3$ heterostructures for high-efficiency catalytic oxidation, Nano Energy. 66 (2019), pp. 104127. https://doi.org/10.1016/j.nanoen.2019.104127.
[48] A. Biswas, S. Saha, S. Pal, N.R. Jana, TiO_2-Templated $BaTiO_3$ Nanorod as a Piezocatalyst for Generating Wireless Cellular Stress, ACS Appl. Mater. 12 (2020), pp. 48363-48370. https://doi.org/10.1021/acsami.0c14965.
[49] B. Jiang, D. Duan, L. Gao, M. Zhou, K. Fan, Y. Tang, J. Xi, Y. Bi, Z. Tong, G.F. Gao, N. Xie, A. Tang, G. Nie, M. Liang, X. Yan, Standardized assays for determining the catalytic activity and kinetics of peroxidase-like nanozymes, Nat. Protoc. 13 (2018), pp. 1506-1520. https://doi.org/10.1038/s41596-018-0001-1.
[50] Y. Chen, L. Jiao, H. Yan, W. Xu, Y. Wu, L. Zheng, W. Gu, C. Zhu, Fe–N–C single-atom catalyst coupling with Pt clusters boosts peroxidase-like activity for cascade-amplified colorimetric immunoassay, Anal. Chem. 93 (2021), pp. 12353-12359. https://doi.org/10.1021/acs.analchem.1c02115.
[51] X. Niu, Q. Shi, W. Zhu, D. Liu, H. Tian, S. Fu, N. Cheng, S. Li, J.N. Smith, D. Du,

Y. Lin, Unprecedented peroxidase-mimicking activity of single-atom nanozyme with atomically dispersed Fe–N_x moieties hosted by MOF derived porous carbon, Biosens Bioelectron. 142 (2019), pp. 111495. https://doi.org/10.1016/j.bios.2019.111495.

[52] Y. Tang, Y. Chen, Y. Wu, W. Xu, Z. Luo, H.-R. Ye, W. Gu, W. Song, S. Guo, C. Zhu, High-indexed intermetallic Pt_3Sn nanozymes with high activity and specificity for sensitive immunoassay, Nano Lett. 23 (2023), pp. 267-275. https://doi.org/10.1021/acs.nanolett.2c04235.

[53] L. Jiao, J. Wu, H. Zhong, Y. Zhang, W. Xu, Y. Wu, Y. Chen, H. Yan, Q. Zhang, W. Gu, L. Gu, S.P. Beckman, L. Huang, C. Zhu, Densely isolated FeN_4 sites for peroxidase mimicking, ACS Catal. 10 (2020), pp. 6422-6429. https://doi.org/10.1021/acscatal.0c01647.

[54] H. Qi, Y. Tong, M. Zhang, X. Wu, L. Yue, Boron-doped and ketonic carbonyl group-enriched graphdiyne as a dual-site carbon nanozyme with enhanced peroxidase-like activity, Anal. Chem. 94 (2022), pp. 17272-17278. https://doi.org/10.1021/acs.analchem.2c04239.

[55] S. Wei, W. Ma, M. Sun, P. Xiang, Z. Tian, L. Mao, L. Gao, Y. Li, Atom-pair engineering of single-atom nanozyme for boosting peroxidase-like activity, Nat. Commun. 15 (2024), pp. 6888. https://doi.org/10.1038/s41467-024-51022-4.

[56] Y. Wang, V.K. Paidi, W. Wang, Y. Wang, G. Jia, T. Yan, X. Cui, S. Cai, J. Zhao, K.-S. Lee, L.Y.S. Lee, K.-Y. Wong, Spatial engineering of single-atom Fe adjacent to Cu-assisted nanozymes for biomimetic O_2 activation, Nat. Commun. 15 (2024), pp. 2239. https://doi.org/10.1038/s41467-024-46528-w.

[57] Y. Li, Q. Wang, X. Qu, J. Tian, X. Zhang, Construction of palladium porphyrins and triptycene photo-activated nanomaterial for enhanced colorimetric detection and inactivation of bacteria, J. Colloid Interface Sci. 648 (2023), pp. 220-230. https://doi.org/10.1016/j.jcis.2023.05.190.

[58] H. Yan, L. Wu, J. Wang, Y. Zheng, F. Zhao, Q. Bai, H. Hu, H. Liang, X. Niu, Target-triggered dual signal amplification based on HCR-enhanced nanozyme activity for the sensitive visual detection of Escherichia coli, Anal. Methods. 16 (2024), pp. 496-502. https://doi.org/10.1039/D3AY01824E.

Supporting Information

Light/Ultrasound Enhance Peroxidase Activity of $BaTiO_3$/graphdiyne/Au Nanozyme for Colorimetric Detection of *E. coli* O157:H7

Di Zhang[a,b], Haoxin Li[a], Kai Wang[a], Yujian Sun[a], Chenguang Wang[a], Yingying Wang[a], Qiang Bai[a,*], Tianzhi Yu[b], Zhugen Yang[c,*], Ning Sui[a,*], Lina Wang[d,*],

[a] College of Materials Science and Engineering, Qingdao University of Science and Technology, 53 Zhengzhou Road, Qingdao, Shandong 266042, China

[b] Key Laboratory of Opto-Electronic Technology and Intelligent Control (Ministry of Education), Lanzhou Jiaotong University, Lanzhou, 730070, China

[c] Faculty of Engineering and Applied Sciences, Cranfield University, Cranfield, MK43 0AL, United Kingdom

[d] College of Environment and Safety Engineering, Qingdao University of Science and Technology, 53 Zhengzhou Road, Qingdao, Shandong 266042, China

[*] Corresponding authors: Q. Bai (baiqiang@qust.edu.cn), Z. Yang (zhugen.yang@cranfield.ac.uk), N. Sui (suining@qust.edu.cn) L. Wang (linawang@qust.edu.cn),

Content

1.1 Raw materials.....4
1.2 POD-like activity test of BGA.....4
1.3 Steady-state kinetic study of BGA.....4
1.4 Free radical scavenging experiments.....5
1.5 EPR testing.....5
1.6 Preparation of BGA-Ab2 immune probe.....6
1.7 Bacterial culture and detection.....6
Fig. S1 TEM images of the (a)BTO and (b)BTO/GDY.....8
Fig. S2 XRD local enlargements of BTO, BTO/GDY, and BGA.....8
Fig. S3 POD-like performance of different material systems under different external field conditions (a) Au@BTO, (b) BTO/GDY, (c) Au@GDY, (d)BTO. 9
Fig. S4 Effect of pH.....9
Fig. S5 Effect of temperature.....10
Fig. S6 Effect of reaction time.....10
Fig. S7 Reaction kinetics curves of BGA under different external field conditions. ..11
Fig. S8 (a) TEM image of BGA. (b) XRD patterns of BGA and BGA (US+Light). (c) XPS spectra of BGA, and BGA (US+Light), (d) C 1 s, (e) Ba 3d, and (f) Ti 2p.....12
Fig. S9 Free radical quenching of BGA. 13
Fig. S10 (a) Piezoelectric and photocurrent response of BGA (b) EIS spectra of BTO, BTO/GDY, and BGA. 13
Fig. S11 (a) phase lag loop, (b) amplitude butterfly loop of BGA. 14
Fig. S12 The horizontal coordinate is the lattice constant of the cell, the vertical coordinate is the total energy of a single cell, and the red line is the range between (a) GDY, and (b) BTO for the stable existence of the cell. 14
Fig. S13 Electron density difference plots for BGA and z-axis values of electron density difference and electron density difference plots of BGA in stretching (left) or compression (right), where positive and negative values represent electron gains and losses. 15
Fig. S14 Surface electric field distribution of BGA under different wavelengths of light. 15
Fig. S15 Radiometric heat map of BGA. (a) Isothermal surface. (b) Body surface temperature. 16

Fig.S16 Colorimetric method for detection of E. coli standard concentration color rendering diagram and corresponding B/(R+G+B) standard line.....16
Table S1 Comparison of reaction kinetic parameters for different catalysts.....17
Table S2 Comparison of reaction kinetic parameters of BGA under different external field conditions.....17
Table S3 Comparison between this biosensor and other methods for detection of *E. coli.* 17

1.1 Raw materials

Polyvinylpyrrolidone (PVP, MW = 1 300 000), anhydrous ethanol(C_2H_6O, 99.7%), acetic acid (HAc, ≥99.5%), barium acetate (≥99%), tetrabutyl titanate ($C_{16}H_{36}O_4Ti$, 98%), tetrahydrofuran (THF, 99.5%), sodium chloride (NaCl, 99.5%), magnesium sulfate ($MgSO_4$, 98%), acetone (≥99.5%), pyridine (C_5H_5N, ≥99.5%), cupric acetate (CuAc, 98%), N,N,N',N'-tetramethylethylenediamine (≥98%), chlorauric acid trihydrate ($HAuCl_4 \cdot 4H_2O$), N,N-dimethylformamide (DMF, ≥99.5%), sodium borohydride ($NaBH_4$, 98%), hydrogen peroxide (H_2O_2, 30%), L-histidine (His), 1,4-benzoquinone (BQ, 98%), isopropyl alcohol (IPA, ≥99.7%) were purchased from Sinopharm Chemical Reagent Co., Ltd. (China). Phosphate buffer saline (PBS), Luria-Bertani (LB) broth, and LB agar powders were purchased from Qingdao Hope Biotechnology Co., Ltd. (China). All aqueous solutions were prepared with ultrapure water (18.25 MΩ cm) supplied by a Milli-Q® system (USA). All bacteria were purchased from Bena Culture Collection, BNCC (China). (*E.coli O157:H7*,*Listeria monocytogenes, Staphylococcus aureus, Vibrio parahaemolyticus, Bacillus cereus, Salmonella typhimurium, and Pseudomonas aeruginosa).*

1.2 POD-like activity test of BGA

3,3′,5,5′-tetramethylbenzidine (TMB) was used as a model substrate to assess the POD-like activity of BGA, during which TMB was oxidized to oxTMB. It' s absorption peak can be measured by measuring the absorbance of oxTMB at 652 nm using a UV-visible spectrophotometer. In this typical experiment, BGA dispersion (100 μg mL^{-1}) was added to an aqueous solution of TMB (1.0 mM) and H_2O_2 (20 mM) in NaAc-HAc buffer (0.1 M, pH 4.0, 1 mL). Light or sonication was applied for 10 min, the absorbance of solution was recorded (note: the absorbance of oxTMB at 652 nm was plotted while defining the highest absorbance value as 100% relative activity).

1.3 Steady-state kinetic study of BGA

BGA dispersion (100 μg mL^{-1}) was added to NaAc-HAc buffer (0.1 M, pH 4.0, 1 mL), and the steady-state kinetics of the BGA were analyzed by either varying the concentration of TMB (0-1.2 mM) and keeping the concentration of H_2O_2 unchanged (20 mM) or by varying the concentration of H_2O_2 (0-28 mM) and keeping the TMB concentration unchanged (1.0 mM) for steady state kinetic analysis.

All reactions were accomplished by detecting changes in absorbance at 652 nm for 10 min. The data were fitted to Michaelis-Menten and Lineweaver-Burk plots using the following equations:

$$v = \frac{V_{max} \times [S]}{K_m + [S]} \quad (1)$$

where v is the initial velocity, V_{max} is the maximum velocity, [S] is the concentration of the substrate, and K_m is Michel's constant.

Specific activity of BGA was measured according to the protocol reported in previous report. The SA was calculated by the following formula:

$$\text{Specific activity} = \frac{V \times (\varepsilon \times l)^{-1} \times (\Delta A / \Delta t)}{m} \quad (2)$$

V is the total volume of the reaction solution (μL). ε is the molar absorption coefficient of the colorimetric substrate, which is typically maximized at 39000 M^{-1} cm^{-1} at 652 nm for TMB. l is the path length of light traveling in the cuvette (cm). ΔA is the absorbance after subtraction of the blank value, and $\Delta A/\Delta t$ is the initial rate of change in absorbance at 652 nm (min^{-1}). m is the nanozyme weight (mg) of each assay.

1.4 Free radical scavenging experiments

BGA (100 μg mL^{-1}) and TMB (1.0 mM) were mixed with different scavengers in NaAc-HAc buffer (1 mL, pH 4.0) (benzoquinone (BQ, 100 μM) to scavenge $\bullet O_2^-$, isopropanol (IPA, 100 μM) to scavenge •OH, L-histidine (His, 100 μM) to scavenge $^1O_2$. Subsequently, H_2O_2 (20 mM) was added to the solution and the reaction was started under light and sonication or without any external field. After 10 minutes of reaction, the solution was centrifuged and the change in absorbance at 652 nm was assessed using a UV-visible spectrophotometer. (Note: The absorbance of oxTMB at 652 nm was plotted when defining the highest absorbance value as 100% relative activity.

1.5 EPR testing

In the EPR experiment, DMPO was used as the scavenger for reactive oxygen species radicals to form DMPO-$\bullet O_2^-$ adduct pairs for $\bullet O_2^-$ detection. BGA (100 μg mL^{-1}) in methanol were mixed with DMPO (50 mM) at 25 °C. After 10 min of combined sonication and light, the samples were vigorously mixed and transferred to quartz tubes for EPR measurement. Similarly, DMPO-•OH adducts are formed in aqueous solution for the detection of •OH. TEMP (50 mM) was used as the scavenger for active oxygen

radicals to form TEMPO-$^1O_2$ adduct pairs for $^1O_2$ detection.

1.6 Preparation of BGA-Ab2 immune probe

The pH of the BGA nanoparticle solution (2 mg/mL) was first adjusted to 7.3, and then, 12 μL of mouse anti-*E.coli* O157:H7 monoclonal antibody Ab2 (1 mg/mL) was added to 1 mL of the BGA nanoparticle solution. After incubation for 60 min at room temperature, 10.0 wt % BSA was added to the mixture and incubation was continued for 30 min. Afterwards, the mixture was centrifuged at 8000 rpm for 10 min and washed twice with 1% PBS containing 1 wt % BSA. Finally, the prepared antibody-modified BGA-Ab2 nanoparticle couplings were collected and suspended in 500 μL of PBS buffer containing 2% BSA and 3% sucrose and stored at 4°C.

1.7 Bacterial culture and detection

E. coli O157:H7 was activated as 1% inoculum and inoculated into broth medium for 20 hours at 37°C (150rpm). 100 μL of the activated culture and 40 mL of LB medium were incubated at 150 rpm for 3 hours at 37°C, where 1 μL was added to 1 mL of 0.85% saline to shake the mixture. Subsequently, 800 μL of the mixture was incubated in 40 mL LB medium at 37 °C and 150 rpm for 8 h to reach a concentration of 10^8 CFU mL^{-1}. All containers and samples in contact with bacteria were sterilised after use.Inspection Platform Inspection Process:*E. coli* O157:H7 was diluted to 50 μL by adding 30 μL of different CFU mL^{-1} (10-10^7) of *E. coli* O157:H7 to a 96-well plate encapsulated with the antibody Ab1 into a solution containing PBS (pH 7.4), 1% BSA, and 0.1% Triton. and BGA was added {(300 μg mL^{-1}), [Ab2] = 12.0 μg/mL}, after incubation for 15 min, the solution was removed and 1 ml of buffer solution with pH=4, 1 mM TMB, 20 mM H_2O_2 was added, and the concentration of E. coli was obtained by identifying the RGB values and comparing them with the standard curve by taking a picture of oxTMB through a smartphone after 5 min of coaction of sonication and light.

1.8 Characterization of materials

The morphology of BGA was observed by transmission electron microscopy (TEM, 2000 FX, JEOL, Japan) and field-emission scanning electron microscopy (FE-SEM, JSM-7500 F, JEOL, Japan). An X-ray photoelectron spectrometer (Thermo Fisher Scientific, USA) equipped with a monochromatic Al Ka X-ray source (Hf = 1486.7 eV) with a take-off angle (TOA) of 45° from the membrane surface. The analyzer spot

diameter was 500 μm. electron binding energy was calibrated with respect to the C1s line at 284.8 eV. Raman spectra were recorded by a Thermo Fischer DXR Raman spectrometer (Thermo Fisher Scientific, USA) at a resolution of 2 cm^{-1} using the 532 nm line of an argon ion laser as the excitation source. The molecular structure of the nanomaterials was determined by Fourier transform infrared (FTIR) spectroscopy (Nikolais iS 10, Thermo Fisher Scientific, USA). pyrroline-N-oxide (DMPO) to capture superoxide anion ($•O_2^-$), hydroxyl radical (•OH), and single linear state oxygen ($^1O_2$). Electrochemical measurements were performed at an electrochemical workstation (PGSTAT 302 N, MetrohmAutolab B. V., The Netherlands). Piezoresponse force microscopy (PFM) was performed on an atomic force microscope (AFM, Bruker Dimension Icon, Germany). An ultrasonic cleaner (40 kHz, 300 W, Kunshan Ultrasonic Instrument Co., Ltd., China) was used to provide mechanical force to generate piezoelectric effect. A UV-visible spectrophotometer (U2700, Hitachi High-Tech, Japan) was used to detect changes in substrate absorbance.

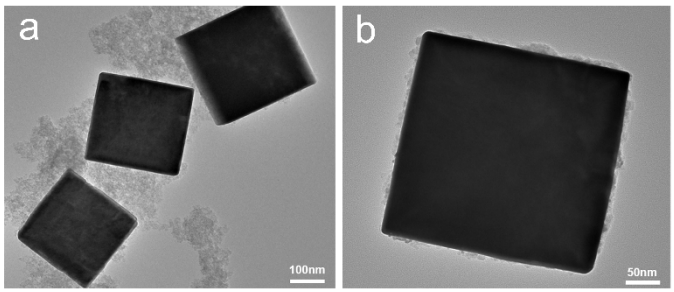


Fig. S1 TEM images of the (a)BTO and (b)BTO/GDY.

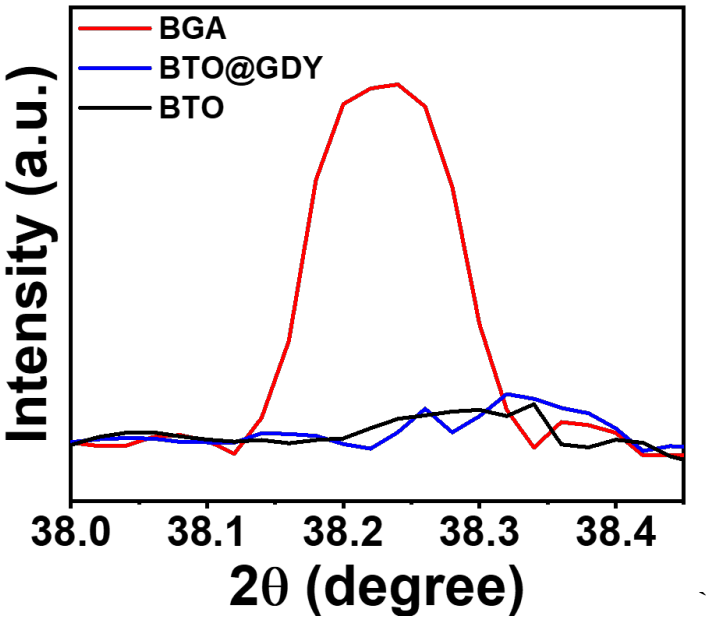


Fig. S2 XRD local enlargements of BTO, BTO/GDY, and BGA.

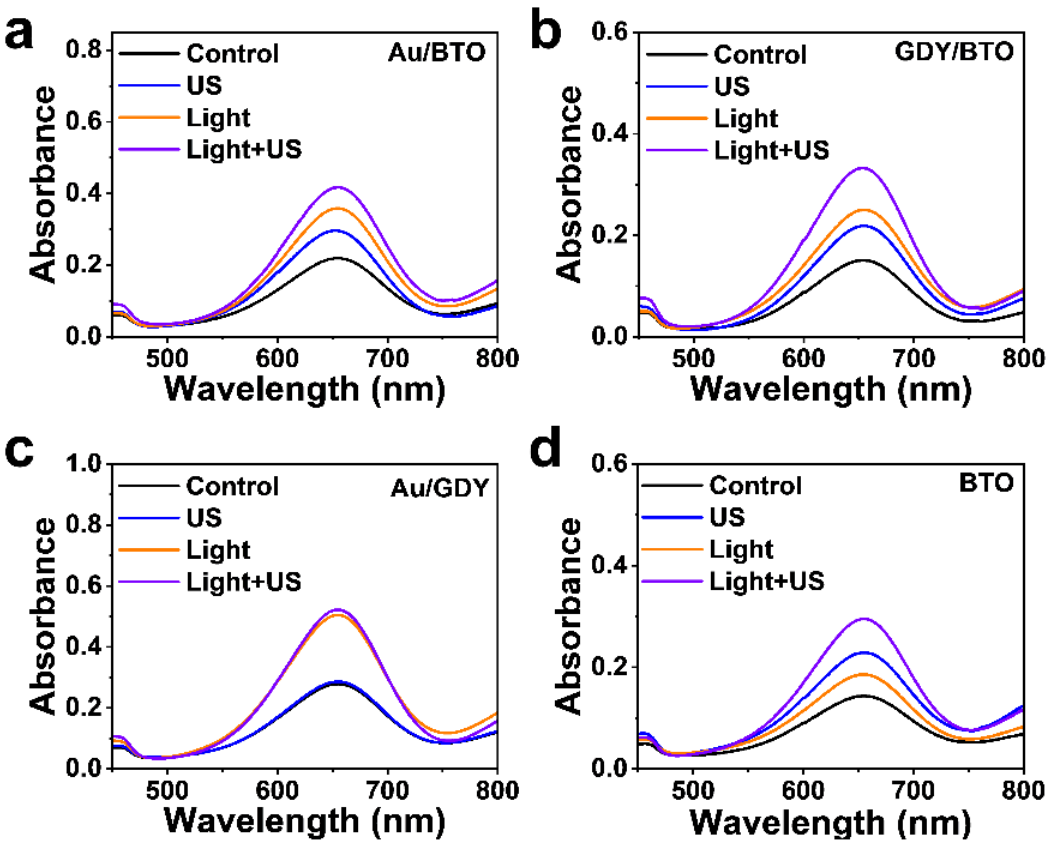


Fig. S3 POD-like performance of different material systems under different external field conditions (a) Au@BTO, (b) BTO/GDY, (c) Au@GDY, (d)BTO.

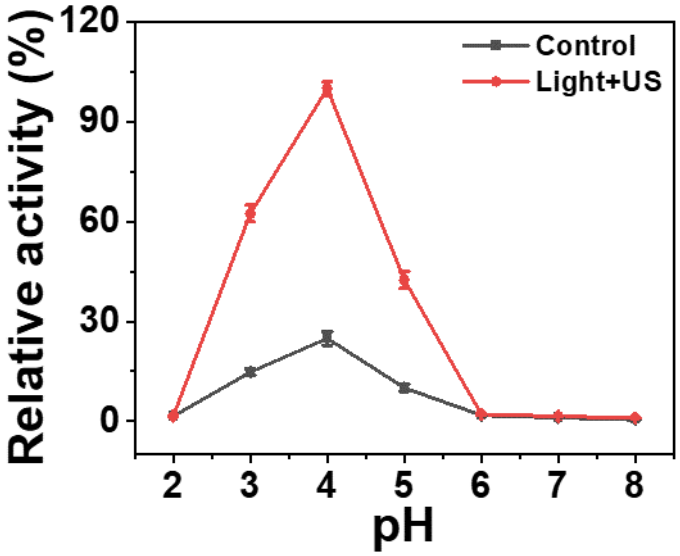


Fig. S4 Effect of pH.

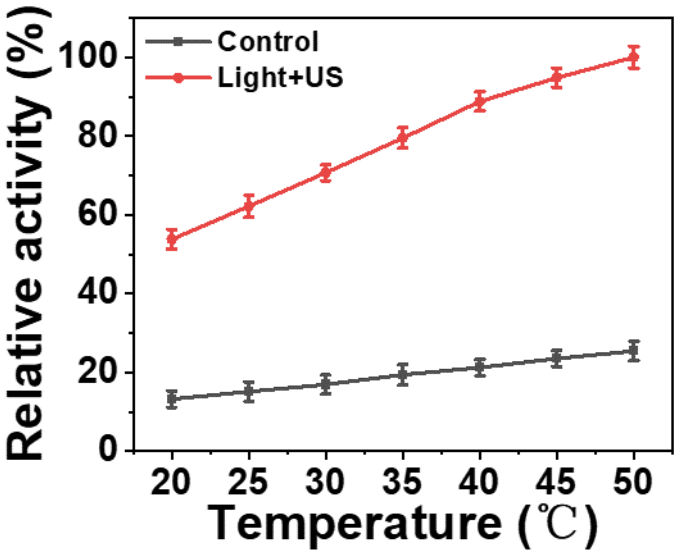


Fig. S5 Effect of temperature.

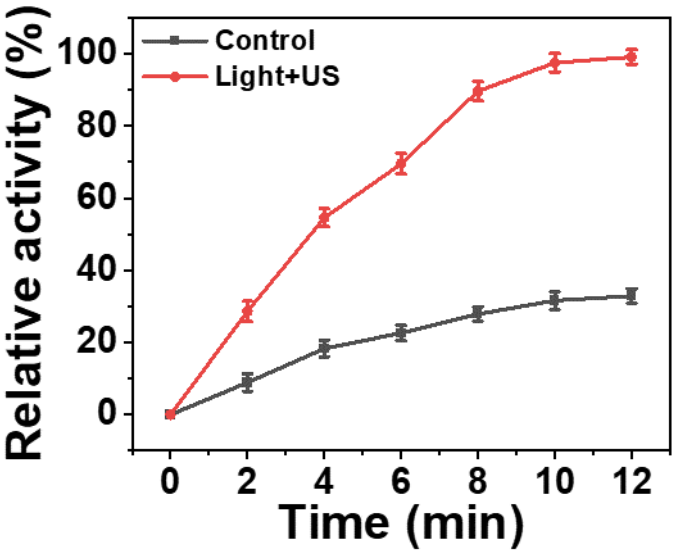


Fig. S6 Effect of reaction time.

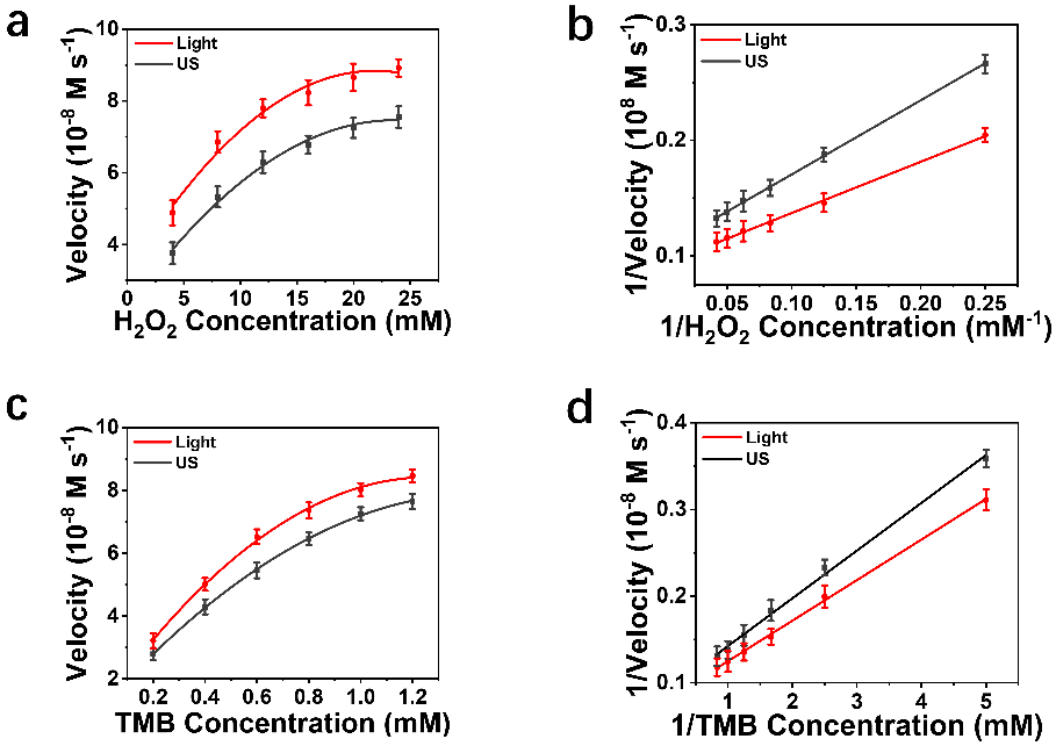


Fig. S7 Reaction kinetics curves of BGA under different external field conditions.

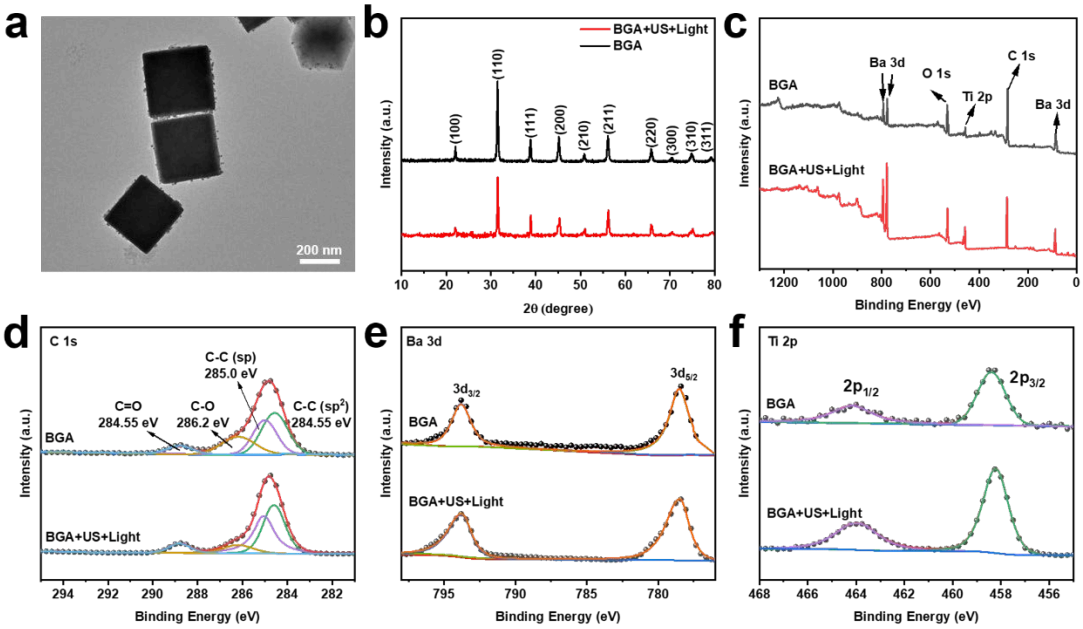


Fig. S8 (a) TEM image of BGA. (b) XRD patterns of BGA and BGA (US+Light). (c) XPS spectra of BGA, and BGA (US+Light), (d) C 1 s, (e) Ba 3d, and (f) Ti 2p.

To fully validate the stability of BGA, we characterized the BGA samples after US, Light, and high-temperature treatment (90 °C), with the results shown in Fig. S8. TEM images (Fig. S8a) indicate that the BGA retained its cubic structure with no significant changes, and the adsorbed Au NPs remained clearly visible. Furthermore, the crystal structure of BGA after combined treatment with US, Light, and high-temperature was analyzed using XRD, as shown in Figure S8b. The diffraction peaks are identical to those of the original BGA, demonstrating the good stability of its crystal structure. Additionally, XPS was employed to further analyze the chemical states of BGA after treatment. The C 1s spectrum (Figure S8d) shows four distinct peaks at 284.5, 285.0, 286.3, and 288.0 eV, corresponding to C-C (sp^2), C-C (sp), C-O, and C=O bonds, respectively. The Ba 3d spectrum (Figure S8e) displays peaks at 779.5 and 794.5 eV, attributed to Ba $3d_{5/2}$ and Ba $3d_{3/2}$, while the Ti 2p spectrum (Figure S8f) shows Ti^{4+} $2p_{3/2}$ and Ti^{4+} $2p_{1/2}$ peaks at 458.4 and 464.2 eV, respectively. These results are in excellent agreement with the structural features of the original BGA, providing strong evidence for the stability of the BGA structure.

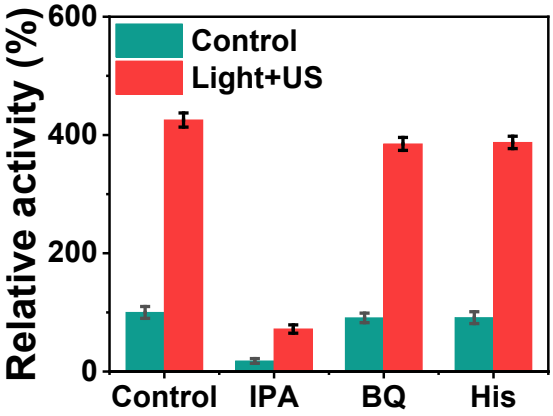


Fig. S9 Free radical quenching of BGA.

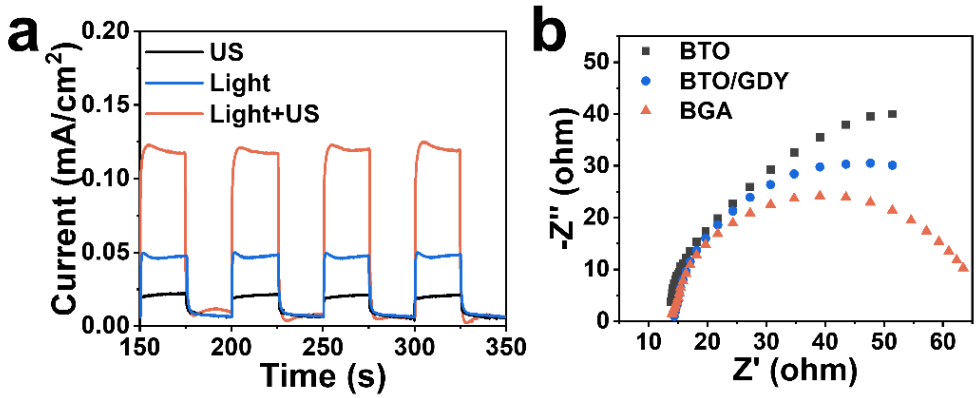


Fig. S10 (a) Piezoelectric and photocurrent response of BGA (b) EIS spectra of BTO, BTO/GDY, and BGA.

The current response of BGA was tested under light and ultrasound stimulation, as shown in Fig. S9a, the current response of BGA under light and ultrasound stimulation was significantly improved, and the saturated current density (0.12 mA/cm^2) was 2.4 times higher than that under light irradiation (0.05 mA/cm^2) and 6 times higher than that under ultrasound stimulation (0.02 mA/cm^2), which indicates that light irradiation and ultrasound help the BGA to produce more free electrons and thus enhance the catalytic activity. Electrochemical impedance spectroscopy (EIS) demonstrated the transfer of charge carriers at the interfacial region of BGA. The relative arc radii of the three materials are BTO > BTO/GDY >BGA (Fig. 9b), which suggests that the BGA have better electrical conductivity and higher interfacial charge carrier transfer efficiency.

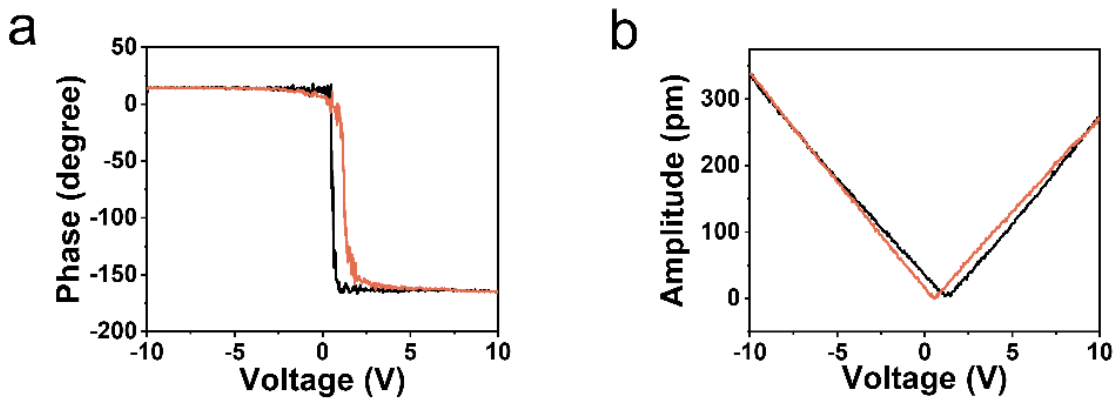


Fig. S11 (a) phase lag loop, (b) amplitude butterfly loop of BGA.

The piezoelectric properties of BGA were investigated by piezoelectric force microscopy (PFM). The phase reversal of the BGA is close to 180°Cafter the 10 V voltage inversion (Fig. S10a), suggesting that it is possible that the dipole moments could be altered by an external electric field. Fig. S10b shows a clear butterfly-shaped amplitude loop of the BGA, illustrating the polarization switching behavior of the BGA under the action of an electric field, which leads to the strain field hysteresis. The slight asymmetry of the piezoelectric amplitude hysteresis loop may be due to the internal magnetic field and the motion of magnetic domains under the tip region. These results indicate that the BGA heterostructure has excellent piezoelectric properties.

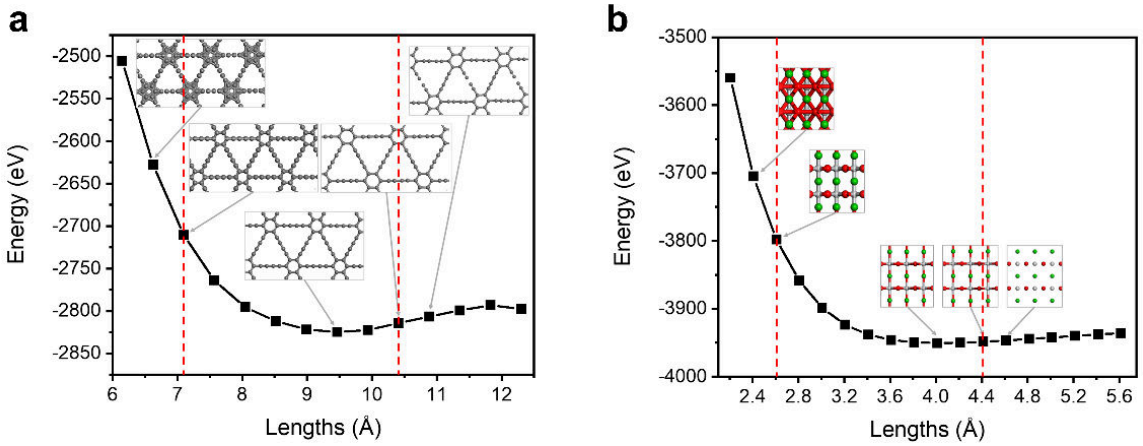


Fig. S12 The horizontal coordinate is the lattice constant of the cell, the vertical coordinate is the total energy of a single cell, and the red line is the range between (a) GDY, and (b) BTO for the stable existence of the cell.

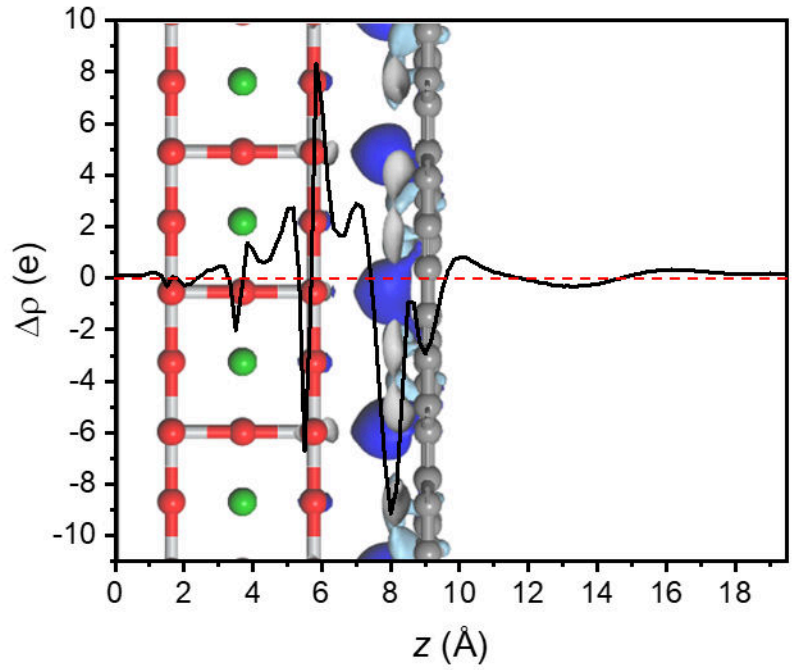


Fig. S13 Electron density difference plots for BGA and z-axis values of electron density difference and electron density difference plots of BGA in stretching (left) or compression (right), where positive and negative values represent electron gains and losses.

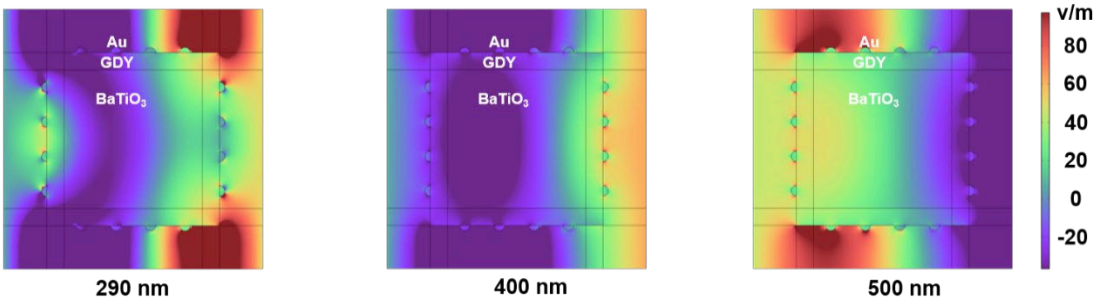


Fig. S14 Surface electric field distribution of BGA under different wavelengths of light.

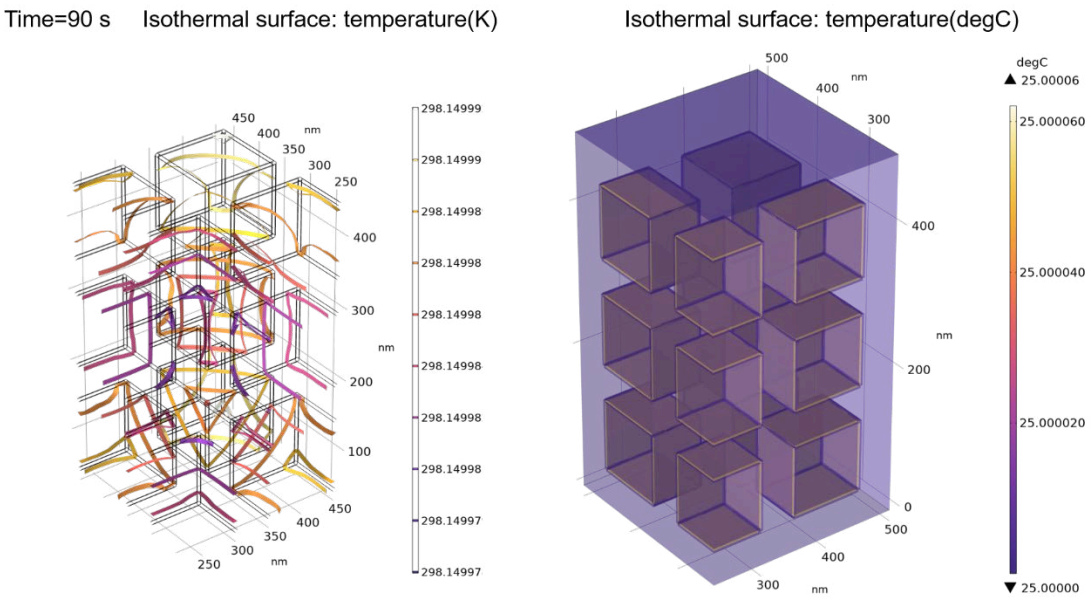


Fig. S15 Radiometric heat map of BGA. (a) Isothermal surface. (b) Body surface temperature.

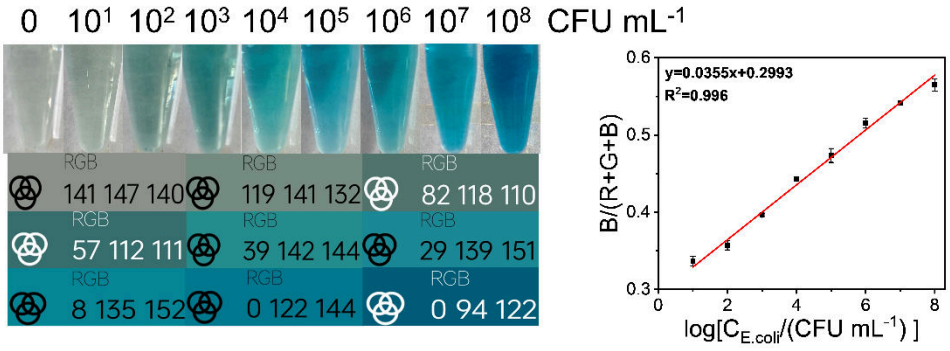


Fig.S16 Colorimetric method for detection of E. coli standard concentration color rendering diagram and corresponding B/(R+G+B) standard line.

Table S1 Comparison of reaction kinetic parameters for different catalysts.

catalysts	K_m (mmol^{-1})		V_{max} (10^{-8} M·s^{-1})		Ref.
	TMB	H_2O_2	TMB	H_2O_2	
BGA(off)	0.30	7.54	6.74	5.72	This work
BGA(on)	0.29	5.83	18.29	18.13	
N-GDQDs/AuAg	0.27	0.72	7.13	10.52	[1]
Au@HCNs	0.03	210	8.63	33	[2]
Ag/rGO	0.85	20.9	3.8	6.23	[3]
Cu-Ag/rGO	0.63	8.62	4.26	7.02	
Ag-Au NC-30@CeO_2		8.5		0.19	[4]
GDYO	0.62	2.59	0.34	0.38	[5]
HRP	0.43	3.70	10.00	8.71	

Table S2 Comparison of reaction kinetic parameters of BGA under different external field conditions.

	blank		light		US		light/US	
	K_m	V_{max}	K_m	V_{max}	K_m	V_{max}	K_m	V_{max}
H_2O_2	7.54	5.72	10.88	8.85	9.59	7.80	5.83	18.13
TMB	0.30	6.74	0.35	10.06	0.47	9.43	0.29	18.29

Table S3 Comparison between this biosensor and other methods for detection of *E. coli.*

Detection platform	Methods	bacterial species	linearity range (CFU mL^{-1})	limit of detection (CFU mL^{-1})	Ref.
HGMF	fluorescence	*E.coli*	8.9-8.9*10^5	14	[6]
Fe_3O_4@SiO_2@PAA	fluorescence	*E.coli*	4-4*10^8	3	[7]
ELISA	colorimetric	*E.coli*	10-10^8		[8]
NFM-MUG	colorimetric	*E.coli*	10^2-10^7	26	[9]
SNP-RB	fluorescence	*E.coli*	10-10^5	8	[10]
Au	colorimetric	*E.coli*	0-10^5	100	[11]
CD@SiO_2	immune adsorption	*E.coli*	0-10^4	2.4	[12]
Fe_3O_4@Au-CP1	colorimetric	*E.coli*	0-10^6	16	[13]
This work	colorimetric	*E.coli*	0-10^7	7	This work

Reference

[1] L. Fan, X. Xu, C. Zhu, J. Han, L. Gao, J. Xi, R. Guo, Tumor catalytic–photothermal therapy with yolk–shell gold@carbon nanozymes, ACS Appl. Mater., 10 (2018) 4502-4511. https://doi.org/10.1021/acsami.7b17916.

[2] G. Darabdhara, B. Sharma, M.R. Das, R. Boukherroub, S. Szunerits, Cu-Ag bimetallic nanoparticles on reduced graphene oxide nanosheets as peroxidase mimic for glucose and ascorbic acid detection, Sensor Actuat. B Chem., 238 (2017) 842-851. https://doi.org/10.1016/j.snb.2016.07.106.

[3] L. Zhang, J. Pan, Y. Long, J. Li, W. Li, S. Song, Z. Shi, H. Zhang, CeO_2-encapsulated hollow Ag–Au nanocage hybrid nanostructures as high-performance catalysts for cascade reactions. Small., 15 (2019) 1903182. https://doi.org/10.1002/smll.201903182.

[4] W. Ma, Y. Xue, S. Guo, Y. Jiang, F. Wu, P. Yu, L. Mao, Graphdiyne oxide: a new carbon nanozyme, Chem. Commun., 56 (2020) 5115-5118. https://doi.org/10.1039/D0CC01840F.

[5] J. Li, F. Yang, X. Chen, H. Fang, C. Zha, J. Huang, X. Sun, M.B. Mohamed Ahmed, Y. Guo, Y. Liu, Dual-ratiometric aptasensor for simultaneous detection of malathion and profenofos based on hairpin tetrahedral DNA nanostructures, Biosens Bioelectron. 227 (2023) 114853. https://doi.org/10.1016/j.bios.2022.114853.

[6] L. Xue, L. Zheng, H. Zhang, X. Jin, J. Lin, An ultrasensitive fluorescent biosensor using high gradient magnetic separation and quantum dots for fast detection of foodborne pathogenic bacteria, Sensor Actuat. B Chem., 265 (2018) 318-325. https://doi.org/10.1016/j.snb.2018.03.014.

[7] R.-R. Hu, Z.-Z. Yin, Y.-B. Zeng, J. Zhang, H.-Q. Liu, Y. Shao, S.-B. Ren, L. Li, A novel biosensor for *Escherichia coli O157:H7* based on fluorescein-releasable biolabels, Biosens Bioelectron., 78 (2016) 31-36. https://doi.org/10.1016/j.bios.2015.11.018.

[8] N. Panchal, V. Jain, R. Elliott, Z. Flint, P. Worsley, C. Duran, T. Banerjee, S. Santra, Plasmon-enhanced bimodal nanosensors: an enzyme-free signal amplification strategy for ultrasensitive detection of pathogens, Anal. Chem., 94 (2022) 13968-13977. https://doi.org/10.1021/acs.analchem.2c03215.

[9] J. Zhang, C. Hurren, Z. Lu, D. Wang, Nanofiber-based colorimetric platform for point-of-care detection of *E. coli*, Chem. Eng. J., 463 (2023) 142357. https://doi.org/10.1016/j.cej.2023.142357.

[10] S.N.A. Jenie, Y. Kusumastuti, F.S.H. Krismastuti, Y.M. Untoro, R.T. Dewi, L.Z. Udin, N. Artanti, Rapid fluorescence quenching detection of escherichia coli using natural silica-based nanoparticles, Sensors Basel., 21 (2021). https://doi.org/10.3390/s21030881.

[11] W. Ren, W. Liu, J. Irudayaraj, A net fishing enrichment strategy for colorimetric detection of *E. coli O157:H7*, Sensor Actuat. B Chem., 247 (2017) 923-929. https://doi.org/10.1016/j.snb.2017.03.090.

[12] Y. Song, G.P. Ostermeyer, D. Du, Y. Lin, Carbon nanodot-hybridized silica nanospheres assisted immunoassay for sensitive detection of Escherichia coli, Sensor Actuat. B Chem. ,349 (2021) 130730. https://doi.org/10.1016/j.snb.2021.130730.

[13] J. Chen, X. Liu, Z. Liu, J. Ma, J. Han, Y. Sun, J. Liang, H. Han, J. Zhao, B. Wang, R. Xiao, Y. Wang, Ultrasensitive SERS biosensor for synchronous detection of *Escherichia coli O157:H7* and pseudomonas aeruginosa via cecropin 1-functionalized magnetic tags-based lateral flow assay, Sensor Actuat. B Chem. 409 (2024) 135598. https://doi.org/10.1016/j.snb.2024.135598.

DSPACE

https://dspace.org/

Light/ultrasound enhance peroxidase activity of BaTiO3 /graphdiyne/Au nanozyme for colorimetric detection of E. coli O157:H7

Zhang, Di; Li, Haoxin; Wang, Kai; Sun, Yujian; Wang, Chenguang ...

2025-05-01
Elsevier
https://doi.org/10.1016/j.snb.2025.137378
Zhang D, Li H, Wang K, et al., (2025) Light/ultrasound enhance peroxidase activity of BaTiO3 /graphdiyne/Au nanozyme for colorimetric detection of E. coli O157:H7. Sensors and Actuators B: Chemical, Volume 430, May 2025, Article number 137378

Downloaded from a DSpace repository. https://dspace.org/